

Causal inference for ~~stratospheric chemistry: insights into~~ quantifying chemical–dynamical pathways controlling tropical middle stratospheric ozone variability

Evgenia Galytska^{1,2}, Birgit Hassler², Carlo Arosio¹, Martyn P. Chipperfield^{3,4}, Sandip S. Dhomse^{3,4}, Kimberlee Dubé⁵, Wuhu Feng^{3,6}, Fernando Iglesias-Suarez², and Jakob Runge⁷

¹University of Bremen, Institute of Environmental Physics, Bremen, Germany

²Deutsches Zentrum für Luft- und Raumfahrt, Institut für Physik der Atmosphäre, Oberpfaffenhofen, Germany

³School of Earth and Environment, University of Leeds, Leeds LS2 9JT, UK

⁴National Centre for Earth Observation, University of Leeds, Leeds LS2 9JT, UK

⁵Institute of Space and Atmospheric Studies, University of Saskatchewan, Saskatoon, Canada

⁶National Centre for Atmospheric Science, University of Leeds, Leeds LS2 9PH, UK

⁷Department of Computer Science, University of Potsdam, Potsdam, Germany

Correspondence: Evgenia Galytska (egalytska@iup.physik.uni-bremen.de)

Abstract.

~~This study investigates the coupling between chemical and dynamical processes driving tropical middle stratospheric~~ Understanding the chemical–dynamical interactions controlling ozone (O_3) variability ~~using a~~ in the tropical middle stratosphere is essential for interpreting short-term trends and their sensitivity to dynamical fluctuations. This study applies a process-oriented causal inference framework that combines causal discovery ~~with and~~ causal effect estimation. This approach integrates qualitative physical knowledge through a causal graph applied to satellite observations and a chemistry-transport model (CTM) simulation. ~~The analysis is split into two subperiods of monthly data : 2004–2011, characterized by an O_3 decrease, and 2012–2018, when O_3 increased in the tropical middle stratosphere,~~ using monthly data for the period 2004–2021. Causal inference identifies distinct processes governing O_3 behaviour. During 2004 ~~robustly identifies a dominant chemical–2011, a~~ robust negative contemporaneous connection from dynamical pathway, in which variability in residual vertical velocity (w^*) modulates nitrous oxide (N_2O), subsequently affecting nitrogen dioxide (NO_2) ~~emerged, while in 2012–2018 this shifted to a one-month lag. This slower response reduced NO~~ and ultimately O_3 . Direct causal effect estimates capture that O_3 variability is dominated by this indirect NO_2 production from–mediated pathway, while the direct influence of w^* on O_3 is weak. The total causal effect (direct and mediated) peaks at a lag of approximately two–three months, indicating that the response develops on this timescale as the influence propagates through N_2O oxidation, limiting O_3 loss via the NO_x catalytic cycle. Further analysis across Quasi-Biennial Oscillation (QBO) regimes reveals regime-dependent differences in the causal links. The and NO_2 . Regime-oriented analysis applied to the observations reveals that the chemical links (N_2O – NO_2 connection is weaker during westerly shear, associated with reduced upwelling, and stronger during easterly shear, reflecting enhanced upwelling, and NO_2 – O_3) strengthen during westerly QBO shear compared to easterly shear.

20 Our study highlights the pivotal role that causal inference can play in disentangling complex chemical-dynamical influences on O₃, complementing traditional statistical methods. This approach lays the foundation for broader applications in stratospheric chemistry, where ~~many relations remain~~ the understanding of various feedback pathways remains uncertain. By discovering and quantifying causal links, this methodology ~~addresses~~ can be adapted to address open questions with environmental and societal relevance. Therefore, integrating causal reasoning into data-driven science enhances process understanding
25 and also strengthens the synergy between machine learning and statistical methods in Earth and environmental sciences.

1 Introduction

Stratospheric ozone (O₃) is essential for protecting life on Earth by absorbing most of the harmful solar ultraviolet (UV-B) radiation (280–315 nm). The tropical ~~middle-stratosphere (10°S–10°N)~~ middle stratosphere (~10 hPa) is a key region for the photochemical formation of O₃ (Chapman, 1930). A balance between photochemical production and loss mainly determines
30 the overall abundance of stratospheric O₃. Meanwhile, its global distribution and inter-annual changes are mainly determined by dynamical and chemical processes in conjunction with their superimposed variability of different origins and periodicity, such as Brewer–Dobson circulation (BDC), El Niño–Southern Oscillation (ENSO) ~~and~~ Quasi-Biennial Oscillation (QBO). ~~Depletion of,~~ concentrations of greenhouse gases (GHGs) and Ozone Depleting Substances (ODSs). Reduction in stratospheric O₃ concentrations causes more UV radiation to reach the Earth’s surface, resulting in harmful effects, including damage to
35 plant life and crops, disruption of aquatic ecosystems, and increased risks of skin cancer, cataracts, immune suppression, and erythema in humans (WMO, 2022; Zerefos et al., 2023). To mitigate these harmful effects, actions taken under the Montreal Protocol (United Nations, 1987) and its Amendments and Adjustments have significantly reduced emissions and atmospheric abundances of ~~ozone-depleting substances (ODSs)~~ ODSs, contributing to the recovery of the stratospheric O₃ layer.

~~According to the recent Scientific Assessment of Ozone Depletion (WMO, 2022) and (Weber et al., 2022; Kuttippurath et al., 2024)~~
40 ~~, aggregated ground- and space-based observations reveal that from 2000 to 2020, Total Column Ozone (TCO) in the tropical region did not show a significant positive trend (0.2 ± 0.3% per decade). This is due to contrasting vertical O₃ trends: stratospheric O₃ levels declined while tropospheric O₃ increased, both trends being unrelated to changes in ODS abundances (WMO, 2022). At the same time, recent studies have highlighted a complex structure in tropical~~

Apparent changes in tropical middle stratospheric O₃ trends can vary substantially depending on the length and timing of the
45 analyzed period. For example, ~~measurements from various satellite instruments consistently show increases in upper-stratospheric in the early 2000s, several studies reported statistically significant~~ O₃ ~~with a positive trend of ~1–1.5% per decade, while a small though uncertain decline (1–2% ± 5% per decade) has been observed in the lower stratosphere (WMO, 2022). The~~ increase in upper-stratospheric ~~decline in this region using a variety of datasets and methodologies (Kyrölä et al., 2013; Eckert et al., 2014; C~~ Subsequent analyses showed that the slight differences in the tropical O₃ ~~results from reductions in ODSs alongside CO₂-driven~~
50 ~~cooling of the stratosphere. Conversely, trends across different data sources arise from small shifts in~~ the ~~lower-stratospheric decrease is linked to~~ analyzed time period, largely due to endpoint anomalies influenced by the ~~climate-change-driven acceleration of large-scale stratospheric circulation (Eyring et al., 2010; Dhomse et al., 2018). This is also supported by Thompson et al. (2021)~~

, who found that ozone trends in the tropical lower stratosphere become insignificant when accounting for tropopause height changes, indicating that chemical ozone loss is not a primary factor in these trends. However, recent work by Villamayor et al. (2023) suggested that halogenated very short-lived substances (VSLS) may account for about a quarter of the observed negative curvature of long-term O_3 trend in the tropical lower stratosphere during 1998–2018. Overall, the current understanding is variability and unaccounted fluctuations in the record (Petropavlovskikh et al., 2019; Sofieva et al., 2021). Recent assessments show that the magnitude of O_3 trends in the tropical stratosphere between around 25–40 km and over 2000–2020 are highly uncertain, with estimates ranging from -2 to 0% per decade across most datasets (WMO, 2022). Earlier studies focusing on the tropical middle (~10 hPa) stratosphere but covering a slightly shorter period (2000–2016) did not reveal a definitive trend across various data sources (Petropavlovskikh et al., 2019; Steinbrecht et al., 2017; Godin-Beekmann et al., 2022). Recently, Arosio et al. (2024) also showed non-significant O_3 trends in the tropical middle stratosphere (2004–2021) below around 35 km based on satellite datasets and the simulations from TOMCAT, a three-dimensional (3-D) chemistry-transport model (CTM, see their Fig. 3). A complementary study by Szelag et al. (2020) reports middle stratosphere since the early 2000s is highly uncertain (-2 to 0% per decade, WMO, 2022) with multiple studies finding no statistically significant or robust long-term trend across different datasets and time periods (Petropavlovskikh et al., 2019; Steinbrecht et al., 2017; Godin-Beekmann et al., 2022; Arosio et al., 2024). In addition, Szelag et al. (2020) highlighted a strong seasonal dependence in tropical middle stratospheric O_3 trends from 2000 to 2018 during 2000–2018, with a significant increase in spring (2–3% per decade) and a non-significant decrease in autumn (-1% to -2% per decade), resulting in overall non-significant trends when averaged across all seasons, which is in agreement, consistent with Galytka et al. (2019); Li et al. (2023). Considering these findings, it is important to note that the slight differences in the tropical O_3 trends across different data sources, arising from small shifts in the analyzed time period, can be attributed to endpoint anomalies influenced by the curvature of O_3 . However, the absence of a persistent long-term trend in recent analyses does not rule out future changes of O_3 variability and unaccounted fluctuations in the record (Petropavlovskikh et al., 2019; Sofieva et al., 2021). The studies mentioned above do not reveal pronounced O_3 trends in the tropical middle stratosphere over extended periods (exceeding approximately 15–20 years), with minor shifts varying by a few years in different directions. This is in contrast to earlier studies reporting a significant decline in O_3 in the early 2000s. Similarly, negative trends observed in the early 2000s. For example, Kyrölä et al. (2013) and Gebhardt et al. (2014) were among the first to detect negative O_3 changes through the analysis of different datasets. Further studies (Eckert et al., 2014; Nedoluha et al., 2015; Galytka et al., 2019) used a variety of datasets and methodologies to confirm the presence of negative O_3 trends. Ball et al. (2018) attributed the observed decrease in tropical middle stratospheric O_3 primarily to high O_3 levels during the 2000–2003 period. However, one might question the relevance of the chemical conditions arise. In this context, understanding the mechanisms governing interannual O_3 decline observed during the early 2000s, given its occurrence over a relatively short time frame and the absence of a similar trend in analyses of the longer periods within the past 20 years. Nonetheless, understanding variability becomes particularly important, as such variability can substantially influence trends derived from a limited observational dataset.

While previously discussed O_3 trends motivate this study, our objective is to quantify the mechanisms that influence control O_3 behavior remains essential, as past trends do not preclude the possibility of their recurrence.

~~To explore the causes of the observed variability on monthly timescales and thus, that can modulate trends over limited time periods. The sensitivity of O₃ decline trends in the tropical middle stratosphere, Galytska et al. (2019) demonstrated that it was ultimately to the analyzed period highlights the dominant role of chemical-dynamical variability in this region. In this context, Galytska et al. (2019) showed that the O₃ decline observed in the early 2000s was dynamically controlled and occurred due linked to increases in nitrogen dioxide (NO₂). The elevated NO₂ levels enhanced O₃ loss through the catalytic NO_x (NO_x = NO + NO₂) cycle, dominant in the middle stratosphere (Portmann et al., 2012). The increase in NO₂, also confirmed by Dubé et al. (2020), resulted from the prolonged residence time of its primary source, nitrous oxide (N₂O). Anthropogenic N₂O is not regulated under the Montreal Protocol (WMO, 2022) and is only addressed by the Kyoto Protocol to the United Nations Framework Convention on Climate Change (UNFCCC). Controlling N₂O emissions would make a major contribution to mitigating long-term climate effects (Nisbet et al., 2021) and stratospheric O₃ depletion (Ravishankara et al., 2009). Over the past 40 years, the rise in atmospheric N₂O has been primarily driven by human-induced emissions, with agricultural sources such as the use of N-fertilizers being the main contributor (Weber et al., 2024). The ongoing increasing levels of N₂O will lead to enhanced NO_x-catalysed O₃ depletion in the middle atmosphere (Chipperfield and Bekki, 2024). Since N₂O is a long-lived species (Portmann et al., 2012; Chipperfield et al., 2014), the changes in its abundance reflect variations in tropical upwelling within the BDC, therefore, they are directly affected by changes in stratospheric transport (Iglesias-Suarez et al., 2021). Prather et al. (2023) showed that during 2005-2021, N₂O increased in the tropical middle stratosphere more than expected from the rate of tropospheric increases. This implied implies a more vigorous BDC, which leads to a shorter lifetime. Minganti et al. (2020) evaluated the climatological impact of the stratospheric BDC on N₂O and reported that, in the tropical middle stratosphere, the interannual variability of vertical residual advection exhibits a significant spread, which reflects the influence of the major source of interannual variability in the equatorial stratosphere, i.e. the QBO on tropical upwelling (Abalos et al., 2015). Chipperfield and Gray (1992), and later Park et al. (2017) highlighted that the source gas N₂O and the reactive nitrogen species (NO_y) display coherent QBO signals within the tropical stratosphere. O₃ also exhibits a strong QBO signal, with the QBO directly influencing O₃ levels by altering the chemical reactions responsible for O₃ depletion, see also Chipperfield et al. (1994) and Ming et al. (2025). This oscillation modulates the rates of these reactions, leading to additional variations in O₃ concentration.~~

~~**Overview of O₃ variability in the tropical (10°S-10°N) middle (10 hPa) stratosphere.** (a) Annual mean anomalies of O₃ for the period 2002-2018. Solid lines represent the sources of the long-term records: OSIRIS (blue), SWOOSH (grey), SAGE-II-SCIAMACHY-OMPS (green), and TOMCAT CTM (orange), with the shaded regions indicating the 95% confidence intervals of the changes. Dashed lines represent simple linear fits for the subperiods 2002-2011 and 2012-2018. (b) Scatter plots of w^* monthly anomalies from reanalysis and N₂O monthly anomalies from observations (circles) and the TOMCAT simulation (triangles), split into the periods 2004-2011 (orange) and 2012-2018 (pink). (c) Same as (b) but for N₂O and NO₂. (d) Same as (b) but for NO₂ and O₃. The Pearson correlations (r) for observations and TOMCAT are indicated above the panels (b-d) for both time periods.~~

~~To Therefore, to set the stage for the analysis of the complex subsequent causal analysis of these chemical-dynamical influences feedback pathways on O₃ variability during 2004-2018, we focus on the deep tropical (10°S-10°N) middle stratosphere (10~~

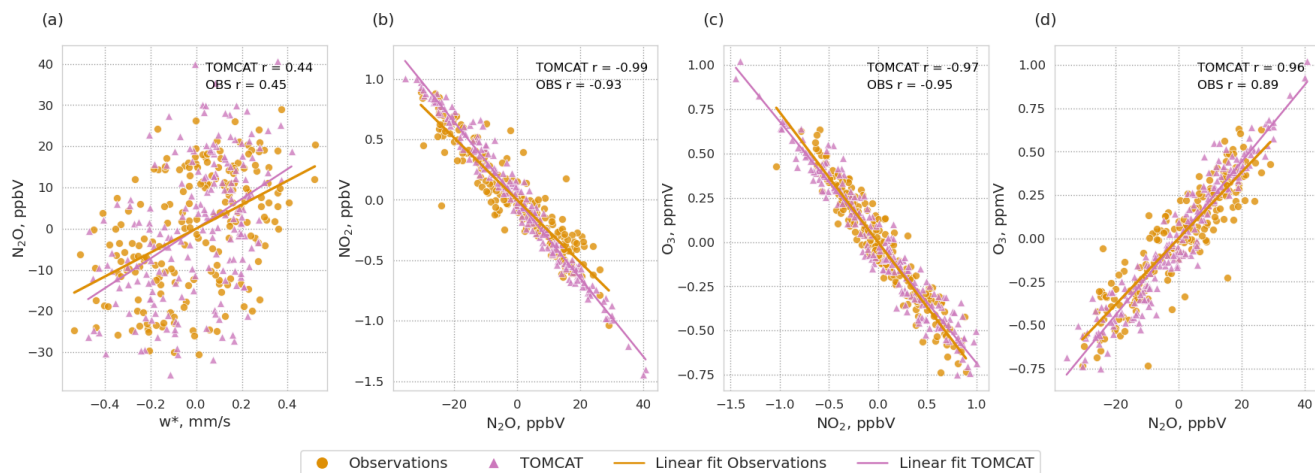


Figure 1. Scatter plots of detrended monthly mean anomalies in the tropical middle stratosphere for 2004–2021, from observations (circles) and the TOMCAT CTM simulation (triangles). Panels show (a) w^* versus N_2O , (b) N_2O versus NO_2 , (c) NO_2 versus O_3 , and (d) N_2O versus O_3 . Solid lines indicate linear regressions for observations (orange) and TOMCAT (pink). The corresponding Pearson correlation coefficients (r) are shown in each panel.

hPa) region. Figure 1 a illustrates the annual mean in the tropical middle stratosphere, Figure 1 presents scatter plots of detrended monthly mean anomalies of (a) residual vertical velocity (w^*) versus N_2O , (b) N_2O versus NO_2 , (c) NO_2 versus O_3 anomalies divided into two distinct periods: 2002–2011, characterized by a decline in O_3 levels (Kyrölä et al., 2013; Gebhardt et al., 2014; E
125 -, and 2012–2018, marked by increasing O_3 , and (d) N_2O versus O_3 levels (Arosio et al., 2019). The analyzed data agree on an overall O_3 decline during 2002–2011 and an increase in the following 2012–2018 period. These contrasting O_3 changes over the two subperiods serve as motivation for the subsequent causal analysis (see Sect. 3) of the processes driving chemical-dynamical interactions in the tropical middle stratosphere. The bi-annual variability in the observed O_3 anomaly time series (Fig. 1a) is
130 associated with the QBO signal. Figure 1b–d shows scatter plots of monthly anomalies for observations and a the TOMCAT CTM simulation for the analyzed subperiods defined in Fig. 1a. Note that the first subperiod is 2004–2011, as N_2O data is not available before this period. 2004–2021. Both observations and the TOMCAT simulations CTM simulation exhibit similar correlations and slopes. The relationship between residual vertical velocity (w^*) and N_2O is moderately positive (panel ba). The strong negative correlations anti-correlations between N_2O and NO_2 (panel e) indicate that b) result from their opposing
135 response to transport-driven variability, where, e.g. enhanced upwelling increases N_2O is the major source of while reducing its chemical loss, which is crucial for NO_2 -, and production (see further discussion in Sect. 4.1). The negative relationship between NO_2 and O_3 (panel dc) is a result of NO_2 being the primary sink of O_3 in the middle stratosphere (Park et al., 2017). The positive relationship between N_2O and O_3 (panel d) is consistent with both tracers exhibiting lifetimes that exceed their vertical transport timescales in this region (Bönisch et al., 2011).

140 While the chemical–dynamical coupling governing tropical middle-stratospheric O₃ is understood, previous research relies mostly on correlation and different types of regression analyses that do not explicitly distinguish between direct and mediated effects within a multivariate system. A causal inference framework proposed in this study represents the relationships between the selected variables as a directed acyclic graph (DAG), in which nodes correspond to physical quantities and edges represent causal influences. Therefore, the structure of the DAG is informed by established physical understanding and subsequently
145 evaluated using causal inference methods applied to the data. Causal inference can then be used to estimate the targeted relationships under explicit assumptions. Applying such an approach to a well-understood chemical–dynamical system provides a reliable test of whether data-driven causal inference can recover known physical pathways and quantify their contributions in the analyzed system. It is important to highlight that to ensure statistical consistency, this study analyzes detrended anomalies rather than long-term trends. Therefore, the results describe variability-driven processes and should not be interpreted as a
150 direct explanation of decadal O₃ trends caused by externally forced long-term changes in CO₂, N₂O emissions, or ODSs, but rather in the context of dynamical processes that are strongly influenced by the QBO.

2 Data sources

This study uses monthly data from satellite observations, reanalysis products, and a TOMCAT CTM simulation, ~~with a focus on the following key variables:~~ focusing on four core variables, namely w^* , N₂O, NO₂, and O₃. ~~We also use the QBO as additional~~
155 variables to examine how the relationships among the four core variables vary under different thermodynamical regimes. By selecting these variables, we focus the analysis on the interpretability of key chemical–dynamical processes that play a major role in controlling O₃ in the tropical middle stratosphere. We intentionally limit the number of variables to maintain a high level of interpretability of the causal graphs. We ~~analyze then later compare the~~ causal graphs from ~~different sources, namely~~ observations and the TOMCAT CTM simulation.

160

2.1 Observations

Since no single satellite instrument provides all the required variables with sufficient temporal and spatial resolution, we integrate data from multiple sources into this study. The following observational or reanalysis-based datasets were used:

- w^* : Derived Transformed Eulerian Mean (TEM) momentum terms (v0.1.1, Serva, 2022), based on ~~ECMWF-European~~ Centre for Medium-Range Weather Forecasts (ECMWF) ERA5 reanalysis (Hersbach et al., 2020) using diagnostics from Serva (2023) Serva (2023); Serva et al. (2024);
- N₂O: Profiles from the Earth Observing System (EOS) Microwave Limb Sounder (MLS)-~~v5.01~~ instrument on NASA's Aura satellite, which offer a vertical resolution of 5–8 km and a horizontal along-track resolution of 165–265 km (Lambert et al., 2020);

- 170 – NO_2 : Profiles retrieved from limb-scattered sunlight observations ~~from on~~ the OSIRIS instrument aboard the Swedish Odin satellite (Murtagh et al., 2002; Llewellyn et al., 2004). OSIRIS NO_2 v7.3 is retrieved via spectral fitting in the 435–477 nm range from 10.5 to 39.5 km with a 2-3 km vertical resolution in most of the stratosphere (Dubé et al., 2022). Due to the pronounced diurnal cycle of NO_2 (Galytska, 2019; Dubé et al., 2020) the photochemical correction from Dubé et al. (2020) was applied to standardize all measurements to a reference time of 12:00 p.m.;
- 175 – O_3 : OSIRIS O_3 v7.3 (Bognar et al., 2022), an improved version of the v5.10 product with corrected long-term drift by accounting for systematic errors in the instrument limb-pointing (Bourassa et al., 2018). ~~SWOOSH v2.7 data (Davis et al., 2016) and merged SAGEH-SCIAMACHY-Ozone Mapping and Profiler Suite (OMPS) (Arosio et al., 2018) were used to illustrate ozone trends in the tropical middle stratosphere over various subperiods in the Introduction in Fig. 1a. Additionally, we used equatorial QBO wind data;~~

~~*ker QBO climatology zonal mean zonal wind taken from the Institute of Meteorology and Climate Research (KIT) for process-oriented analysis based on different QBO phases in Fig. ??, see~~

~~The combination of ERA5 w^* , MLS N_2O , and OSIRIS NO_2 and O_3 In the following, the combination of these datasets is collectively referred to as "observations".~~

2.2 TOMCAT Chemical Transport Model

185 TOMCAT is a three-dimensional off-line CTM (Chipperfield, 2006), driven here by winds and temperatures from the ERA5 reanalysis (Hersbach et al., 2020). Given prescribed atmospheric transport and temperature fields, TOMCAT calculates the distributions of chemical species in the troposphere and stratosphere. A stratospheric full-chemistry simulation, including all of the NO_y chemistry discussed in this paper, was run at a horizontal resolution of $2.8^\circ \times 2.8^\circ$ with approximately 1.5 km vertical resolution in the stratosphere (Chrysanthou et al., 2025). The model uses time varying sulfate aerosol surface

190 area density Dhomse et al. (2015), solar fluxes (Dhomse et al., 2016), and lower boundary concentrations of GHGs and ODSs (WMO, 2022), recommended for CMIP6 simulations. We used the monthly average output in our analysis. The TOMCAT CTM simulation was chosen for its ability to provide a continuous time series without spatial or temporal gaps, making it ideal for robust comparison with the observational datasets.

2.3 Data preprocessing

195 Monthly anomalies ~~were calculated with respect to the 2004–2018 climatology of w^* , N_2O , NO_2 , and O_3 in the tropical (10°S–10°N) middle (10 hPa) stratosphere for selected variables, namely w^* , N_2O , NO_2 and O_3 were calculated~~ from observations and the TOMCAT CTM simulation ~~relative to the climatological mean over August 2004–December 2021. The analysis begins in August 2004, due to the availability of MLS N_2O observations. However, for simplicity, we refer to the period as 2004–2021. To maintain a robust comparison against temporal sampling discrepancies,~~ TOMCAT CTM data were

200 masked to align with observations, omitting any dates with missing observational data. For causal inference, all time series were standardized. Since the application of causality requires the stationarity of the time series (see Sect. 3.1), we remove the

linear trend from all analyzed time series. [For more details about preprocessed timeseries from observations and the TOMCAT CTM simulation and their further comparison, see Appendix A.](#)

3 Methods

205 3.1 Causal inference

We apply the latent Peter-Clark momentary conditional independence (LPCMCI) algorithm (Gerhardus and Runge, 2020), which is an extension of the PCMCI+ algorithm specifically designed to deal with latent (i.e. unobserved) variables (Runge et al., 2019; Runge, 2020). LPCMCI employs ideas from the Fast Causal Inference (FCI) algorithm to learn not only directed causal relationships but also infer the presence of latent confounders (Spirtes, 1995). LPCMCI benefits from the same ideas
 210 underlying PCMCI+ by increasing the effect size of conditional independence (CI) tests through including causal parents in conditioning sets. The LPCMCI method seeks to learn a Directed Partially Ancestral Graph (DPAG), which captures the causal relationships among the observed variables. Contrary to Maximal Ancestral Graphs (MAGs) that contain directed arrows (\rightarrow) and bidirected edges (in other words, double-headed arrows \leftrightarrow), PAGs can include additional edge types. These edges, drawn as $\circ\rightarrow$ and/or $\circ-\circ$, indicate the presence of hidden variables or uncertainty about the exact causal direction.

215 To understand the causal structure of the underlying complex dynamical system, the observed time series $\mathbf{X}_t = (X_t^1, \dots, X_t^N)$, where N stands for the different variables represented by time series, is assumed to follow the following causal process:

$$X_t^j = f_j(\mathcal{P}(X_t^j), \eta_t^j),$$

where f_j is a measurable function that depends on all its inputs, η_t^j represents dynamical noise (independent across $t' \neq t$). Here, $\mathcal{P}(X_t^j) \subset \mathbf{X}_{t+1}^- = (\mathbf{X}_t, \mathbf{X}_{t-1}, \dots) \setminus \{X_t^j\}$ denotes the set of parent variables of X_t^j since the value of X_t^j is determined
 220 from the variables in $\mathcal{P}(X_t^j)$ and the dynamical noise η_t^j . Bidirected links between X_t^i and X_t^j in this model imply that the associated noise terms η_t^i and η_t^j are dependent through unobserved confounding. We assume causal stationarity, meaning $X_{t-\tau}^i \in \mathcal{P}(X_t^j)$ if and only if $X_{t-\tau-\Delta t}^i \in \mathcal{P}(X_{t-\Delta t}^j)$. In practice, causal discovery algorithms ~~such as LPCMCI, including LPCMCI,~~ require approximately stationary time series ~~to,~~ [meaning time series whose statistical properties, such as mean and variance, remain approximately constant over time. Nonstationary behavior, such as long-term trends, can introduce spurious](#)
 225 [statistical dependencies and bias CI tests, leading to incorrect causal links. Therefore, removing or accounting for such trends \(via masking or sliding window\) is a methodological necessity to](#) ensure that the ~~estimated conditional dependencies are not biased by nonstationary trends.~~ [We](#) algorithm identifies causal relationships associated with the internal dynamics of the system rather than coincidental alignment of long-term shifts in the variables (Runge et al., 2019, 2023).

[Additionally, we](#) also assume the absence of cyclic causal relationships, which, due to the temporal order, limits interactions
 230 to contemporaneous cases only when $\tau = 0$. Furthermore, we assume the standard assumptions of constraint-based causal discovery, the Markov condition and the faithfulness condition (Spirtes et al., 2000; Runge et al., 2023), which implies that conditional independence in the observed distribution generated by the ~~SCM above implies d-separation~~ [structural causal model](#)

above implies directional separation (i.e. separation of variables by conditioning on appropriate sets of other variables) in the associated time series graph and vice versa.

235 We conducted a series of sensitivity tests with various settings of α_{pc} and τ_{max} , but only used the causal graphs ~~for~~ with $\alpha_{pc}=0.02$ and $\tau_{max} = 1$ for the toy model (see Sect. 4.1), ~~observations, and with $\alpha_{pc}=0.05$ and $\tau_{max} = 2$ for the observations~~ and the TOMCAT CTM simulation (see Sect. 4.2). Since some of the analyzed variables have non-gaussian distributions, we use the RobustParCorr conditional independence test, which transforms the data to a normal distribution before the partial correlation test. This usage implies that we assume the functions f_j in the model above to be linear. As a trade-off to its ability
 240 to also deal with latent confounding, LPCMCI suffers from lower recall compared to, e.g., PCMCI+ (Runge, 2020). Despite this, LPCMCI successfully identified causal connections in observational data that align closely with expert knowledge and the literature review. ~~Note, however, that we included one link assumption in this study, namely that the residual vertical velocity w^* does not directly influence O_3 . For the process-oriented analysis (Sect. ??) we further assumed that N_2O has no direct influence on O_3 . These links were left out of the initialization of the LPCMCI method.~~ However, LPCMCI did not robustly
 245 detect anticipated connections in the TOMCAT CTM simulation. To estimate the direct causal effects for the ~~three (sub)periods~~ period 2004-2021 in the TOMCAT CTM simulation, we refined the causal graphs by incorporating expert knowledge and insights from the literature review (as further discussed in Sect. 3.3 and depicted in Fig. 2).

3.2 Causal effect estimation

Over a hundred years ago, Wright (1921) suggested a method to estimate causal effects in linear models. This approach
 250 estimates the so-called path coefficients for all links in causal paths and then sums the products of these path coefficients over all causal paths. This method applies only to ~~directed acyclic graphs (DAGs)~~ DAGs; therefore, in the case of DPAG, we ensure that all edges are directed before applying causal effect estimation. Causal effect estimation consists of the following steps:

1. For all causal links $i \rightarrow j$ that belong to causal paths from X to Y (where X is a parent and Y is a child), estimate the
 255 path coefficient $\beta_{i \rightarrow j}$ by regressing j on all its parents and taking the coefficient corresponding to parent i . 2. The causal effect is then computed as:

$$CE = \sum_{\text{causal paths}} \prod_{\text{link } i \rightarrow j \text{ in path}} \beta_{i \rightarrow j}$$

By restricting this estimator to paths that pass through at least one node among a selected set of mediators M^* , it is also possible to compute mediated causal effects (MCE). These are defined as:

$$260 \quad MCE = \sum_{\text{causal paths through at least one } M \in M^*} \prod_{\text{link } i \rightarrow j \text{ in path}} \beta_{i \rightarrow j}$$

3.3 Process-oriented causal inference framework

~~To advance the understanding of~~

To quantitatively characterize O₃ variability in the tropical middle stratosphere during ~~the 2004-2018 period and the two subperiods defined in Fig. 1a (2004-2011 and 2012-2018)~~2004-2021, we employ a process-oriented causal inference approach depicted in Fig. 2. Although causal analysis has already gained significant application in atmospheric sciences, including the analysis of Arctic processes and their links to middle latitudes (Polkova et al., 2021; Docquier et al., 2022; Galytska et al., 2023; Kretschmer et al., 2020), teleconnections (Karmouche et al., 2023; Tibau et al., 2022; Carvalho-Oliveira et al., 2024), atmosphere-biosphere interactions (Krich et al., 2020), and evaluating climate models (Nowack et al., 2020; Debeire et al., 2025) and their sensitivities (Ricard et al., 2024), it has not yet been applied to the study of stratospheric chemical-dynamical interactions.

Figure 2 outlines the process-oriented causal inference framework, which is built upon three essential components (blue squares): (1) a causal graph that contains information about qualitative cause-and-effect relationships (Runge et al., 2023), (2) observational and/or modeled data, and (3) a method for estimating causal effects. To construct (1) the causal graph, we employ a triangulated approach (Denzin, 2010; Uleman et al., 2024) that integrates (i) expert knowledge, (ii) a comprehensive literature review, and (iii) a data-driven causal discovery algorithm. While each of these components can independently contribute to the creation of the causal graph, we recommend employing the triangulated approach to ensure a more robust and reliable framework. To assess the performance of the selected (iii) causal discovery algorithm before applying it to real-world data, we first construct a (iv) "toy model" using synthetic data. This synthetic dataset is designed to replicate the properties and challenges of the real system while incorporating known underlying ground truth from (i) expert knowledge and (ii) a literature review. The toy model is then used to evaluate the performance of the causal discovery method in realistic, finite sample scenarios (Camps-Valls et al., 2023). To ensure the robustness of the results, it is recommended to further perform sensitivity tests on free algorithm parameters, such as α_{pc} and τ_{max} for (iii) the causal discovery algorithm and (iv) the toy model.

It is important to note that if (iii) the causal discovery algorithm does not robustly detect anticipated relationships in the analyzed (2) real-world or modelled data, the causal graph may be constrained based on (i) expert knowledge and (ii) a comprehensive literature review, including previous successful applications of causal discovery to related research topics. The final (1) causal graph, derived from (2) real-world data, serves as a foundation for estimating (3) direct and total causal effects. Causal effect estimation can be further refined through a process-oriented analysis, such as, for example, masking on different atmospheric regimes. Additionally, (v) total causal effects can be assessed across different time lags. This complex approach outlined in Fig. 2 ensures robust and reliable causal inference, particularly for complex systems such as the stratospheric chemical-dynamical interactions investigated here.

3.4 Confidence intervals and masking for regime-oriented analysis

Confidence intervals for direct causal effect estimates, computed using Wright's path coefficient (Sect. 4.2), were obtained via bootstrapping with 500 members. Only significant direct causal effects are shown, defined as when the bootstrap confidence interval does not include 0. For both direct and total causal effects across different time lags (Sect. 4.4), confidence intervals were likewise obtained from 500-member bootstrapping.

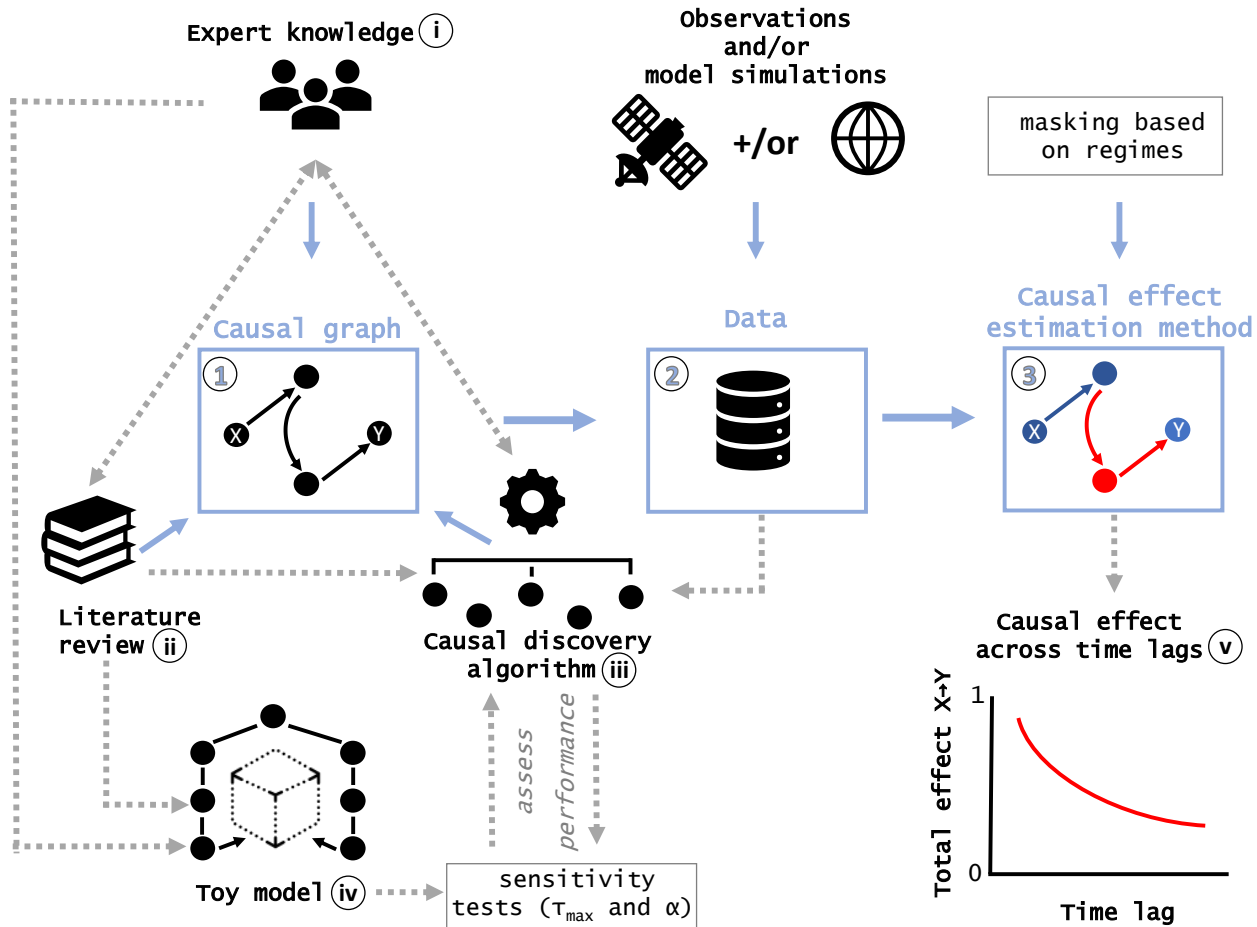


Figure 2. Process-oriented causal inference framework built upon three essential components (blue squares): (1) a causal graph, (2) data, and (3) a method for causal effect estimation. To construct the (1) causal graph for the studied system, a triangulated approach (Uleman et al., 2024) is applied, integrating (i) expert knowledge, (ii) a literature review, and (iii) a data-driven causal discovery algorithm. Before applying the (iii) causal discovery algorithm to real-world data, we construct a (iv) toy model to assess the performance of the selected (iii) causal discovery algorithm. The final (1) causal graph, based on (2) real-world data, serves as a foundation for estimating (3) causal effects, which can be further refined through process-oriented analysis, including masking on atmospheric regimes and additional sensitivity tests.

For the regime-oriented analysis of causal effects during different QBO phases (Sect. ~~??~~4.3), we first calculate the QBO wind shear as the ~~zonal wind gradient~~ vertical gradient of the zonal mean zonal wind between 10 hPa and ~~12 hPa~~ log-pressure coordinates 30 hPa. For observations, the shear is derived directly from radiosonde-based zonal wind at the two pressure levels (Kerzenmacher and Braesicke, 2026). For the TOMCAT CTM simulation, the zonal wind is first averaged over 10°S–10°N before computing the vertical gradient between 10 and 30 hPa. The resulting shear time series is subsequently standardized for use in the process-oriented causal analysis. Positive (negative) values correspond to a westerly (easterly) shear zone, which plays a central key role in modulating secondary circulation and stratospheric transport. We focus on the ~~10-12~~ 10-30 hPa shear layer since no data is available above 10 hPa in the used observational record.

4 Results and Discussions

305 4.1 Causal justification and validation with a toy model

Before applying causal discovery to ~~investigate~~ analyze chemical–dynamical interactions ~~in the tropical middle stratosphere~~ using observations and ~~TOMCAT model simulations~~ the TOMCAT CTM simulation, we first summarize the relationships of O₃ variability in this region in a shape of DAG-based on expert knowledge and literature review (as discussed and interpreted by e.g. Galytska et al., 2019; Nedoluha et al., 2015), following the procedure discussed in Sect. 3.3. Figure 3a depicts a simple
310 linear chain from the cause w^* to the outcome O₃ (grey nodes), with mediating variables N₂O and NO₂ (magenta nodes). The inferred DAG, therefore, represents an effective causal structure that emerges under the influence of dynamical variability, rather than a representation of isolated chemical relationships. In particular, a positive relationship from w^* to N₂O (labelled A) indicates that an increase in residual vertical velocity leads to enhanced N₂O concentrations. The relationship from N₂O to NO_x (labelled B) is negative, despite N₂O being a source of NO_x. This apparent contradiction is an example of Simpson’s paradox (Blyth, 1972) and arises because upwelling tropical residual velocity w^* acts as a confounding ~~factor~~ dynamical process, leading to an ~~anticorrelation~~ anti-correlation between N₂O and NO₂. Namely, slower (faster) upwelling results in lower (higher) N₂O concentrations and consequently longer (shorter) N₂O residence time in this region, which allows more (less) time for the photochemical production of NO_x from N₂O. ~~It is important to note that w^* does not exert a direct causal influence on NO_x, instead, its effect is mediated through N₂O.~~ Consequently, higher (lower) NO_x levels lead to lower (higher) O₃ concentrations via the
320 NO_x-catalyzed ~~ozone~~ O₃ destruction cycle, resulting in a negative relationship ~~(labelled C)~~ (labelled C, see Crutzen, 1970). Table 1 summarizes the discussed chemical-dynamical relationships in the tropical middle stratosphere as depicted in Fig. 3a.

We further justify the assumed causal DAG in Fig. 3a and validate the reliability of the causal inference method. For that, we require a benchmark dataset with known causal ground truth for validation as depicted in Fig. 3a. We consider the linear structural causal process with four time series as an example that comes from a data-generating process using the following
325 model:

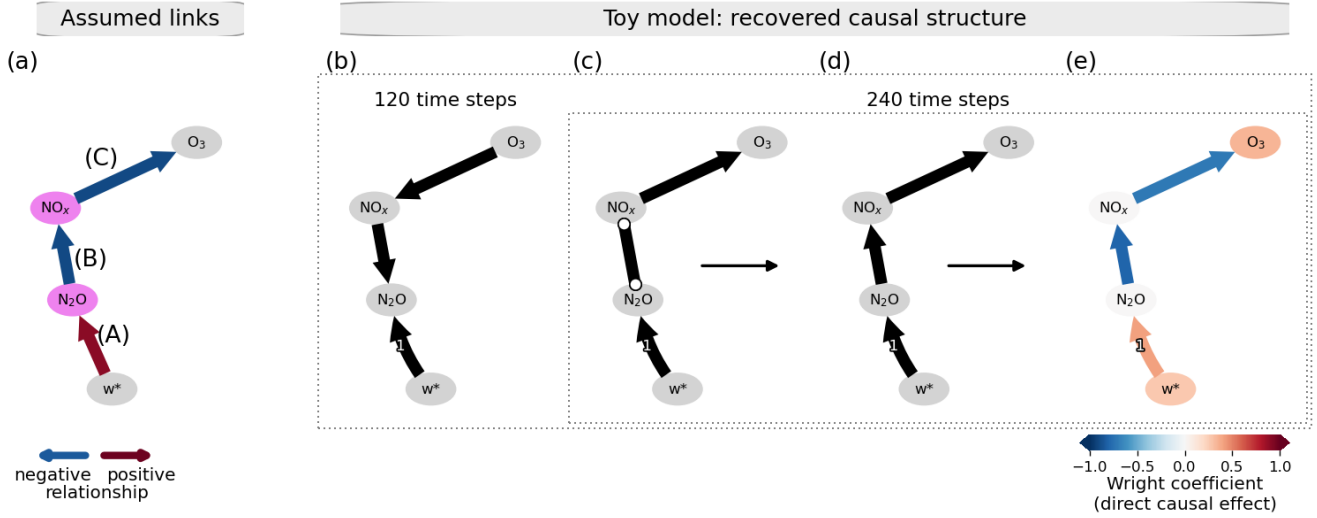


Figure 3. Causal justification and validation. (a) Assumed relationships based on expert knowledge and literature review. Magenta nodes indicate mediators in the total influence of w^* on O_3 . (b-e) Causal discovery applied to a generated toy model with contemporaneous (time lag = 0) and lagged (time lag > 0) dependencies based on linear partial correlation as a conditional independence test for 120 time steps (b) and 240 time steps (c), which corresponds to the DPAG. The application of the triangulated approach from Fig. 2 resulted in the DAG (d), which in turn was used as a basis for causal effect estimation, where edge colors indicate the estimated direct causal effects (e).

$$\begin{aligned}
 X_t^0 &= 0.3X_{t-1}^0 + \eta_t^0 \\
 X_t^1 &= 0.3X_{t-1}^1 + 0.4X_{t-1}^0 + \eta_t^1 \\
 X_t^2 &= 0.3X_{t-1}^2 - 0.94X_t^1 + \eta_t^2 \\
 X_t^3 &= 0.3X_{t-1}^3 - 0.95X_t^2 + \eta_t^3
 \end{aligned} \tag{1}$$

where η_i stands for the independent Gaussian white noise processes with variances σ^2 , X^0 depicts residual vertical velocity w^* , X^1 - the concentration of N_2O , X^2 - NO_x , X^3 - O_3 . This set of variables and their dependencies define a toy model. Although this toy model is designed to replicate causal dependencies in the tropical middle stratosphere, it is important to emphasize that there are multiple approaches to constructing such a model. While additional variables could be further introduced based on expert knowledge and a thorough literature review, the goal of the analysis here is not to maximize the number of variables but to create an intuitive system that can simply and effectively replicate the processes under study.

Figure 3b-e illustrates the causal graphs inferred from the causal discovery algorithm (see Sect. 3.1) when applied to the toy model from Eq. (1). To evaluate the performance of the causal discovery algorithm on time series of different lengths, Fig. 3b,c show causal graphs for generated time series of 120 timesteps-time steps (equivalent to 10 years of monthly data) and 240 timesteps-time steps (equivalent to 20 years), respectively. When applied to the shorter time series (Fig. 3b), causal discovery fails to detect several expected connections as anticipated from Fig. 3a, likely due to limitations in the toy model, such as weaker

Table 1. Summary of chemical-dynamical processes in the tropical middle stratosphere.

Label in Fig. 3a	Connection	Link type	Description
A	$w^* \rightarrow \text{N}_2\text{O}$	positive	Transport is the primary source of stratospheric N_2O . In addition to determining N_2O concentrations (an increase of w^* leads to an increase of N_2O), it also affects its residence time (an increase in w^* leads to a shorter residence time of N_2O).
B	$\text{N}_2\text{O} \rightarrow \text{NO}_x$	negative	N_2O is the primary source of NO_2 via the slow reaction $\text{N}_2\text{O} + \text{O}(^1\text{D}) \longrightarrow 2\text{NO}$ followed by the rapid reaction $\text{NO} + \text{O}_3 \longrightarrow \text{NO}_2 + \text{O}_2$. As N_2O increases due to a faster circulation, its residence time decreases, and therefore, NO_2 concentrations decline (there is less time to produce NO_2). <u>The resulting link is therefore negative. In the absence of dynamical variability, the relationship would appear positive, reflecting only the underlying chemical production of NO_2 from N_2O.</u>
C	$\text{NO}_x \rightarrow \text{O}_3$	negative	NO_2 is the primary sink of O_3 in the tropical middle stratosphere via the NO_x catalytic cycle.

causal signals or higher noise. In contrast, despite the plausible limitations of the toy model, most expected connections are recovered in the 20-year time series depicted in Fig. 3c. However, the inferred graph lacks directionality between N_2O and NO_2 (shown as $\circ-\circ$ edge), resulting in a DPAG. Since causal effect estimation requires a fully directed DAG, we applied the triangulation approach to resolve ambiguities, yielding the DAG in Fig. 3d. This final causal graph (Fig. 3d) serves as the basis for causal effect estimation, shown in Fig. 3e. Given approximately linear relationships among analyzed variables (see Fig. 1b-d), we assume linear causal effects and apply Wright’s method (Wright, 1921). This approach is akin to linear regression slopes between two variables X and Y, with the critical distinction that the graph is used to detect and eliminate confounding influences before regression (see Sect. 3.2 and Fons et al., 2023).

4.2 Physical description of observed and modeled causal relations

Figure 4 presents the magnitude and sign of direct causal effects computed using Wright’s approach (Wright, 1921) on causal graphs identified by the triangulation (Uleman et al., 2024) based on observations (top row) and the TOMCAT CTM simulation (bottom row) over the full period b) during 2004–2018 (panels a, d) and two subperiods: 2004–2011 (panels b, e) when O_3 declined, and 2012–2018 (panels c, f) when O_3 increased. Across all three periods, 2021. The original graphs inferred by the causal discovery algorithm (see Sect. 3.1) without the application of the triangulated approach are shown in Appendix B. The causal discovery algorithm successfully identifies the anticipated connections in the observations (Fig. 4a-e) since the signs of the direct causal effects align well with the expected processes outlined in the Introduction and as discussed in Sect. 4.1.

Notably, the positive lagged ~~links in observations in analyzed periods (panels a-c) link in observations~~ from w^* to N_2O ~~indicate indicates~~ that an increase in residual vertical velocity intensifies N_2O transport. This enhanced transport, in turn,

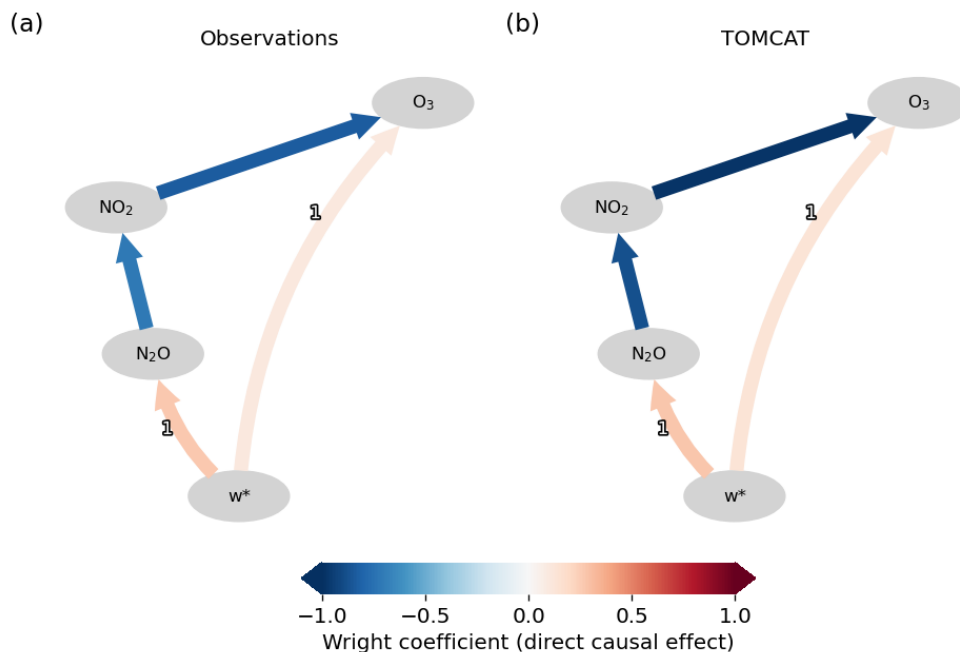


Figure 4. Causal inference: Magnitude and sign of the direct causal effects. The direct causal effects calculated for the observations (top row a) and the TOMCAT CTM simulation (bottom row b) from the detrended monthly anomalies for the full period 2004-2018 (panels a and d), 2004-2011 (panels b and e), and 2012-2018 (panels c and f) 2004-2021. For TOMCAT, the causal graphs identified from the observations were used, and direct causal effects were then estimated with the TOMCAT data. Straight arrows show the contemporaneous (time lag = 0) connections; curved arrows indicate lagged links (time lag > 0); edge color stands for the estimated direct causal effects. For TOMCAT, causal graphs identified from the observations were used, and direct causal effects were estimated using the TOMCAT data.

reduces the residence time of N_2O , leading to less time for NO_2 production via the reaction $N_2O + O(^1D) \longrightarrow NO + NO$ (also labelled B in Fig. 3a). Consequently, the causal contemporaneous link from N_2O to NO_2 reflects the negative relationship confounded by upwelling. Notably, during 2012–2018 the algorithm detected this N_2O to NO_2 connection at a one-month lag (and not contemporaneous at lag zero), indicating that to O_3 indicates that lower/higher NO_2 production occurred with a delay compared to 2004–2011 (panel b). This does not rule out the existence of a contemporaneous connection, but instead suggests that the lagged relationship was statistically more robust during that period. The emergence of this one-month lagged connection in the relationship from N_2O to NO_2 points to a shorter N_2O residence time, consistent with faster transport in 2012-2018 compared to the earlier period, as further supported by levels are associated with higher/lower O_3 concentrations, as O_3 loss in the tropical middle stratosphere is largely driven by catalytic NO_x destruction. Causal discovery further detects a bidirected connection between w^* changes calculated with the Long-term Ozone Trends and Uncertainties in the Stratosphere (LOTUS) regression model shown in Appendix ?? and O_3 in the observations, indicating the presence of a latent common driver of w^* and O_3 and that neither variable is an ancestor of the

other (see Appendix B, Fig. ??a-c. ~~Additional sensitivity tests confirm the robustness of the B1a~~). As causal effect estimation requires a DAG, we define the direction from w^* to O_3 to quantify the strength of this link. This choice allows us to estimate the direct dynamical influence of w^* on O_3 , which is sometimes identified by a causal discovery algorithm in sensitivity tests. Based on Fig. 4, the direct influence of w^* on O_3 is much weaker, and a mediated pathway via N_2O ~~to and~~ NO_2 ~~lagged connection in 2012–2018 compared to the contemporaneous connection observed in 2004–2011 (see Appendix ??, Figs. ?? and ??)~~. Additionally, ~~the negative contemporaneous link dominates~~. However, temperature-mediated effects could amplify the apparent strength of the connection from NO_2 to O_3 ~~indicates that lower/higher NO_2 levels result in higher/lower O_3 concentrations, as~~, since enhanced upwelling induces both cooling (increasing O_3 ~~loss~~) and reduced NO_x species. To assess this, we performed additional analysis, including temperature anomalies in the tropical middle stratosphere ~~is largely driven by catalytic NO_x destruction (Crutzen, 1970)~~. The inferred graph structure was not robust, likely because w^* is a derived diagnostic that depends on thermodynamic fields. Removing w^* altered the parent structure and prevented a direct comparison of direct causal effects shown in Fig. 4a. We therefore interpret the identified NO_2 -mediated pathway as the dominant mechanism, while acknowledging that temperature-related effects may potentially project onto this link.

Unlike the observations, ~~the causal discovery algorithm was unable to identify the expected connections~~ in the TOMCAT CTM simulation, ~~as anticipated from the expected processes~~ the causal discovery algorithm does not fully reproduce the expected chemical-dynamical coupling as outlined in the Introduction, Sect. 4.1 and as shown in Fig. 4a-c. ~~The reasons for this limitation are a.~~ In particular, the anticipated one-month lagged link from w^* to N_2O is not robustly detected. We found that this occurs because O_3 exhibits very strong contemporaneous coupling with both N_2O and NO_2 , such that conditioning on O_3 makes the one-month lagged w^* to N_2O link statistically insignificant. As further demonstrated and discussed in Appendix ??-B, this does not indicate a lack of dynamical coupling in the TOMCAT CTM simulation. Instead, it reflects the strong shared variability among the chemical tracers as the model uses a chemically consistent scheme for all the variables. To still assess the strength of the processes represented in TOMCAT, we did not rely on the TOMCAT-derived graph. Instead, ~~we applied the graph identified from the observations and used it as a fixed structure to~~ by adopting a fixed graph structure derived from observational ground truth and expert knowledge, we can accurately estimate direct causal effects with the TOMCAT data (Fig. 4d-f)b), providing a valid and pragmatic solution for quantifying model sensitivities. Similar to observations, the direct one-month lagged w^* - N_2O connection is estimated as significant in the TOMCAT CTM simulation for the analyzed ~~periods~~ period. Additionally, N_2O - NO_2 ~~links are negative contemporaneous link is~~ slightly stronger in the TOMCAT CTM simulation (~~panels d and e~~ Fig. 4b) compared to those in the observations (~~panels a and b~~ Fig. 4a), with a similar causal pattern observed for the NO_2 - O_3 link. ~~During 2012–2018 the strength of the~~

To ensure the robustness of the detected in Fig. 4a connections in observations in the tropical middle stratosphere during the period 2004–2021, Fig. 5 demonstrates the results of the application of the causal discovery algorithm with different setups of τ_{max} (depicted on the x-axis) and α_{pc} (depicted with markers). τ_{min} set to zero to account for the contemporaneous connections. It should be noted that choosing a τ_{max} that is too low risks missing causal links with longer delays, which violates the assumption of causal sufficiency. However, choosing τ_{max} too high without mitigation can dilute the detection power of the causal algorithm. Specifically, a larger τ_{max} expands the search, as the algorithm tests more possible lagged pairs.

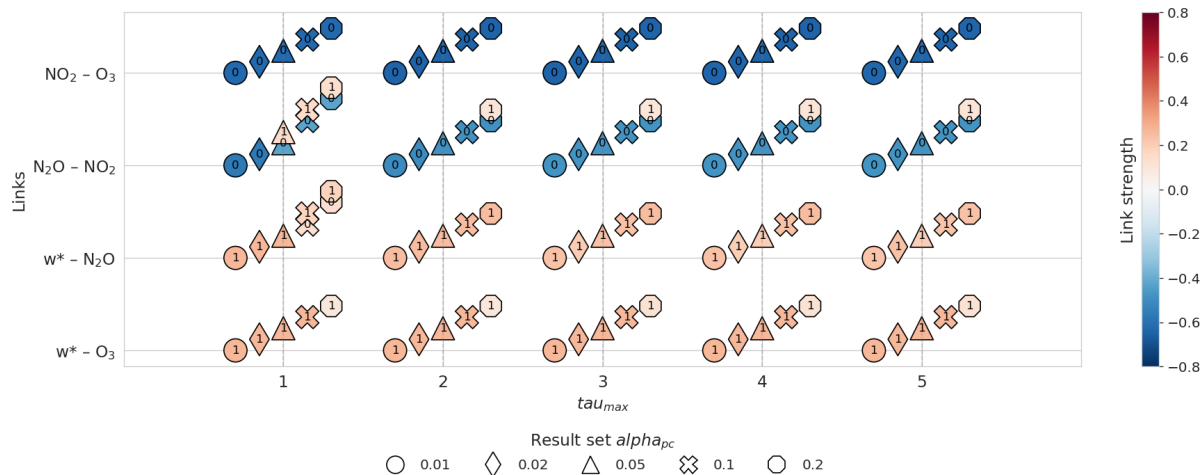


Figure 5. Sensitivity tests of the detected links to the choice of τ_{max} (x-axis) and α_{pc} (depicted with markers) for the observations for the period 2004–2021. For all tests $\tau_{min} = 0$. Only link pairs shown in Fig. 4 are considered.

This leads to larger conditioning sets, which can further reduce the effect size and detection power. Therefore, it is important to condition only on a few relevant variables that actually explain the relationship (Runge et al., 2019). Sensitivity tests from Fig. 5 show very similar results for different configurations of τ_{max} and α_{pc} . The chemical connections related to N_2O - NO_2 and NO_2 - O_3 pairs are robustly detected as contemporaneous across all experiments. The dynamical connections w^* - N_2O and w^* - O_3 are robustly detected with a one-month lag.

A further analysis of the sensitivity experiments reveals an additional feature in the N_2O - NO_2 relationship. A positive one-month lagged link from N_2O to NO_2 is detected across all tested τ_{max} , but primarily at relaxed significance thresholds ($\alpha_{pc}=0.2$). For $\tau_{max}=1$, the link is also identified at $\alpha_{pc}=0.1$ and 0.05 . Such a positive lagged connection is physically plausible, as NO_2 is produced from N_2O , as discussed in Table 1, and a delayed response may emerge at the monthly timeseries. However, given its sensitivity to the choice of α_{pc} , this link cannot be considered a robust pathway.

4.3 Process-oriented analysis

We adopt the process-oriented causal analysis (Nowack et al., 2020; Karmouche et al., 2023; Eyring et al., 2024; Debeire et al., 2025) to major drivers of tropical middle stratospheric O_3 variability to further understand the robustness of the connections during different regimes. Given that N_2O , NO_2 , and O_3 exhibit a strong QBO signal (Chipperfield et al., 1994; Tian et al., 2006; Park et al., 2017; ...), we mask the data to easterly and westerly shear zones (see Sect. 3.4). This approach makes it possible to explore the regime-dependent robustness of causal relationships. A robust connection between specific variables indicates that the particular link is consistently detected across multiple resampled datasets. A robust connection also suggests that the relationship is less sensitive to variations in the data, providing higher confidence that the detected connection is not a result of random fluctuations or sampling variability. It is also important to note that the analyzed period includes an unprecedented QBO disruption in 2016

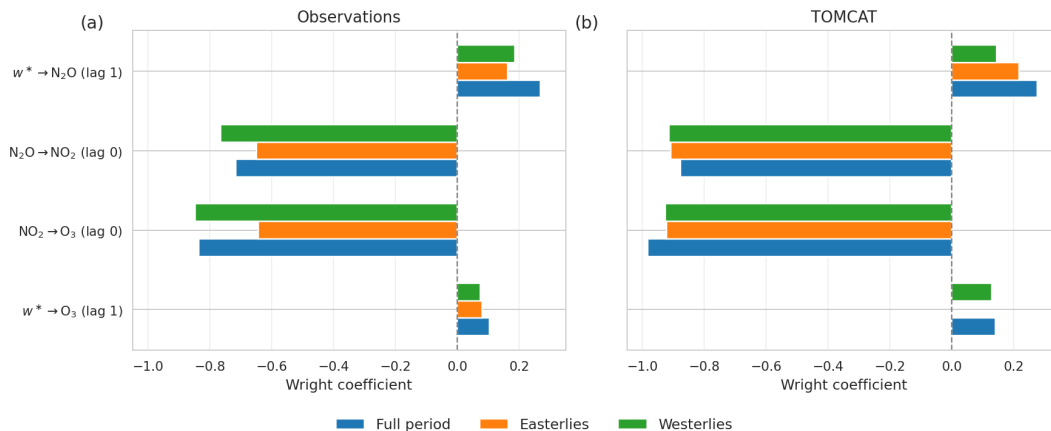


Figure 6. Regime-oriented direct causal effects from observations (a) and the TOMCAT CTM simulation (b) for the full 2004-2021 period (blue), and for easterly (orange) and westerly (green) QBO regimes.

(Tweedy et al., 2017; Match and Fueglistaler, 2021), which stalled the descent of the easterly shear toward 10 hPa and caused anomalous upwelling and wind patterns, temporarily altering transport and mixing in the tropical middle stratosphere. To assess how QBO phase affects the strength of the identified relationships, we keep the causal graph inferred from the full period and re-estimate the link strengths separately for easterly and westerly QBO conditions. This approach isolates regime-oriented changes in coupling strength without altering the underlying network structure. Figure 6 illustrates the estimated direct causal effects for both observations (panel a) and the TOMCAT CTM simulation (panel b) for the full period 2004-2021 (blue), which also corresponds to direct causal effects shown in Fig. 4a,b, easterly (orange), and westerly phase of the QBO.

The dynamical positive link from w^* to N_2O at a lag of one month shows slightly reduced magnitude in observations when separating into QBO phases compared to the full period. In the TOMCAT CTM simulation, the link strength is similar to the observational one (panel a), highlighting the agreement between different data sources observations and also slightly reduces across QBO phases. The negative contemporaneous chemical coupling between N_2O and NO_2 is stronger in the TOMCAT CTM simulation compared to observations and of similar strength across phases. In observations, the absolute magnitude is slightly larger during the westerly phase than during the easterly phase. The contemporaneous negative link from NO_2 to O_3 is likewise stronger in the TOMCAT CTM simulation compared to the observations. In the observations, this link weakens during the easterly QBO phase, whereas in the TOMCAT CTM simulation its magnitude is comparatively stable across QBO phases.

The imposed one-month lagged connection from w^* to O_3 is the weakest among the analyzed pathways and substantially smaller than the chemically mediated pathway. In the TOMCAT CTM simulation, no link is detected for the easterly QBO phase. This phase-dependent absence of this connection points to its limited robustness. This also indicates that the direct influence of the residual circulation on O_3 variability is predominantly mediated through N_2O and NO_2 , rather than through a direct dynamical effect. Overall, the sign of all connections is robust across datasets and QBO phases. In the observations, the chemical links (from N_2O to NO_2 and from NO_2 to O_3) tend to strengthen during the westerly QBO phase.

4.4 Causal effects across different time lags

While the causal discovery algorithm, along with causal effects estimation of the direct links, offers a general overview of whether the methodology captures the expected dependencies, one can further study the propagation of causal effects through the causal graph across different time lags. The total causal effects (for further discussions, see Appendix C), which are not necessarily just depicted by a single arrow in the causal graph, can be derived from direct causal effects using Wright's path analysis for specific relationships across different time lags. Figure 7 shows total ~~and direct (lines) and direct (labels)~~ causal effects across different time lags for a selection of different (X, Y) pairs of variables, where a positive connection, similar to Fig. 4, indicates that an increase in X leads to an increase in Y after a time lag (τ). Due to the limited number of variables in the causal graphs, we do not analyze the role of mediators for specific connections, as their influence is straightforward. For example, the total effect from w^* to NO_2 is mediated solely by N_2O , as shown in Fig. 4. However, for the analyses that involve more complex causal graphs, similar to Fons et al. (2023), we recommend estimating the contribution of various mediators on a specific set of connections.

~~The total and direct~~ Figure 7 demonstrates that the total causal effects across different time lags in the TOMCAT CTM simulation (dashed lines) closely align with observations ~~across analyzed periods (solid lines) across analyzed regimes, indicating that the model reproduces not only the sign but also the temporal structure of the effects.~~ However, the ~~causal effects amplitudes~~ in the TOMCAT CTM simulation are slightly ~~stronger than those in observations, particularly for the effect of larger,~~ suggesting a somewhat stronger coupling between analyzed variables in the simulation. The direct effect of w^* on other variables (see dashed lines in Fig. 7a-c). The direct causal effect of residual vertical velocity w^* on the transport of N_2O into the stratosphere (Fig. 7a) ~~reveals a peak in the positive connection exhibits a clear maximum~~ at a lag of four months in the observations and the TOMCAT CTM simulation across all three periods. The total effect around three months for the full period 2004–2021 and during the easterly QBO phase. This peak defines the characteristic adjustment timescale of dynamical transport. The total effects of w^* on NO_2 (Fig. 7b) and on O_3 (Fig. 7c and Appendix C) ~~, both clearly mediated by also reach their~~ maxima at approximately three months, consistent with a sequential mediation through N_2O ~~, reaches its maximum at a lag of approximately 3–4 months in both cases. This indicates the timeframe within which w^* must act to influence these chemical constituents. Observations and the TOMCAT CTM simulation agree that the total effect of w^* on and subsequently NO_2 and O_3 during the 2012–2018 period (Fig. 7b,e) is delayed and significantly weaker than in other periods. This reduced total effect from.~~ We can further decompose the total effect of w^* on NO_2 and O_3 indicates weaker connections between the variables, potentially due to factors such as a shorter residence time of N_2O , leading to a lower NO_2 production and, as a result, O_3 into direct and indirect contributions. As shown by Fig. 4a and Fig. 6a, the direct one-month lagged w^* on the O_3 increase (shown in Fig. 1a and consistent with changes from Fig. ??).

The N_2O on NO_2 relationship (Fig. 7d) shows close alignment for the subperiods 2004–2011 and 2012–2018, particularly after a lag of two-three months, with pathway is approximately 0.10 in the observations and 0.14 in the TOMCAT CTM simulation detecting slightly weaker relationships. This suggests no significant differences in the influence of. The indirect contribution, mediated via N_2O on and subsequently NO_2 after a lag of two-three months in both subperiods. However, the

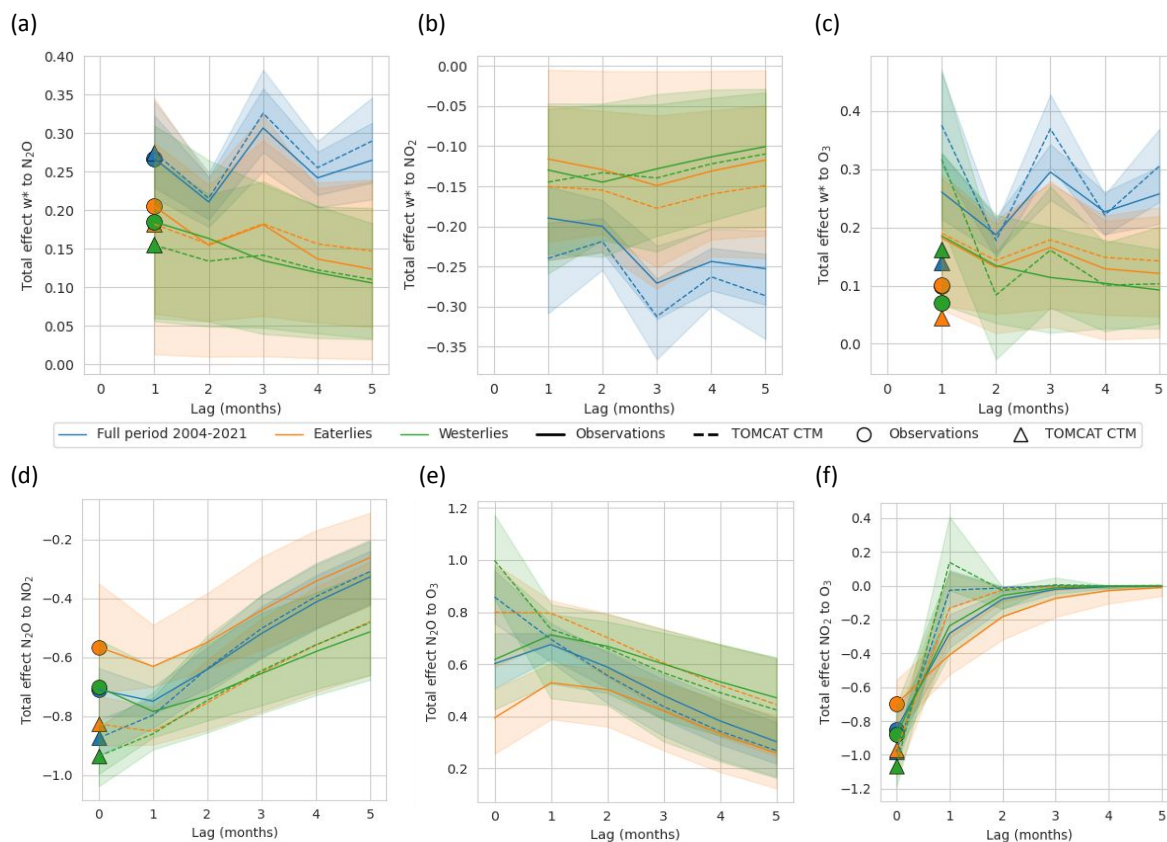


Figure 7. Total ~~and direct~~ causal effects across different time lags (in months) from observations (solid lines) and the TOMCAT CTM simulation (dashed) for (a) w^* on N_2O , (b) w^* on NO_2 , (c) w^* on O_3 , (d) N_2O on NO_2 , (e) N_2O on O_3 , (f) NO_2 on O_3 . All plots show the results obtained for 2004-2018-2004-2021 (blue), 2004-2011-easterly (orange), and 2012-2018-westerly QBO phase (green). The markers indicate direct causal impact presented in Fig. 4 and 6. The shading corresponds to the 90% bootstrap confidence interval. ~~In panel (f), the blue and green curves largely overlap, and therefore only the blue line is visible.~~

largest differences are observed at lags prior to two months, where the more significant connection for the period 2012-2018 first appears at lag one and is stronger between lags one and two compared to the 2004-2011 period. This pattern is related to the N_2O - O_3 causal relationship (Fig. 7e), where the total influence of N_2O reaches 0.16 in the observations and 0.23 in the simulation (not shown here). Therefore, the total effect of w^* on O_3 is delayed by one month.

The NO_2 on O_3 relationship (shown in Fig. 7f) peaks at lag zero in both observations and the TOMCAT CTM simulation, consistent with fast chemical reactions. Notably, this is the only connection where the effect decays rapidly, reaching near-zero values at c at a lag of one month for the full period 2004-2018 and 2012-2018 and around three months for the 2004-2011 period. The longer persistence of the causal effect of NO_2 on O_3 provides direct evidence of extended exposure of O_3 to the NO_x catalytic cycle, contributing to the ozone decline observed during 2004-2011 (also shown in Fig. 1).

The specific causal relationships across different time lags provide insights into the observed changes in the analyzed species (Appendix D further discusses lagged dependencies of causal effects). The changes in analyzed variables were also investigated using the LOTUS regression model, with a discussion provided in Appendix ???. By comparing and combining the causal inference approach (including causal effects across different time lags) with the LOTUS regression model, we link the one-month delayed influence of w^* on O_3 through N_2O and NO_2 mediators during the period 2012–2018 to the observed increase in O_3 levels (see Appendix ??, Fig. ??). This increase is a consequence of the delayed NO_x production from N does not alter the magnitude of the mediated effect, indicating that the dominant indirect pathway proceeds sequentially through w^* , N_2O , which is consistent with the negative trend in NO_2 (Fig. ??h). In contrast, during 2004–2011, the N_2O – NO_2 relationship at lag zero was stronger, leading to a higher production of NO_x species at lag zero compared to 2012–2018, which explains the positive trend in NO_2 during 2004–2011 (Fig. ??g).

Process-oriented causal effect estimation

We adopt the process-oriented causal analysis (Nowack et al., 2020; Karmouche et al., 2023; Eyring et al., 2024; Debeire et al., 2025) to major drivers of tropical middle stratospheric N_2O and O_3 variability to further understand the robustness of the connections during various regimes. Given that,

The N_2O , NO_2 , and O_3 exhibit a strong QBO signal (Chipperfield et al., 1994; Tian et al., 2006; Park et al., 2017), apart from splitting the analyzed time period to 2004–2011 and 2012–2018, we also mask the data to westerly and easterly shear zones in the tropical middle stratosphere (see Sect. 3.4). This approach makes it possible to explore the regime-dependent and period-specific robustness of causal relationships. A robust connection between specific variables indicates that the particular connection is consistently detected across multiple resampled datasets. A robust connection also suggests that the relationship is less sensitive to variations in the data, providing higher confidence that the detected connection is not a result of random fluctuations or sampling variability. It is also important to note that the 2012–2018 period includes an unprecedented QBO disruption in 2016 (Tweedy et al., 2017; Match and Fueglistaler, 2021), which stalled the descent of the easterly shear toward 10 hPa and caused anomalous upwelling and wind patterns, temporarily altering transport and mixing in the tropical middle stratosphere.

Regime-oriented direct causal effects from observations for the complete 2004–2018 period (middle panel) and corresponding regimes. Each graph is labelled with the total number of data points (months) characterized by each regime. Similar to Fig. 4, the color of the arrows indicates the value of the direct causal effect. All nodes shown in grey were hypothesized to be auto-dependent with a lag of one.

Figure ?? summarizes the causal graphs derived from the observations. The central causal graphs resemble those from Fig. 4a–c. To refine the process-oriented analysis, we further masked the data according to easterly and westerly wind shear regimes within the 2004–2011 (top) and 2012–2018 (bottom row) periods. It should be noted that the shorter subperiods may limit the robustness of causal discovery, and the corresponding sample sizes are therefore indicated in brackets for each regime.

520 For instance, during easterly wind shear in 2012–2018, only 19 months of data were available, preventing the detection of meaningful causal connections.

Figure ?? shows a positive one-month lagged connection from w^* to N_2O relationship (Fig. 7d) strengthens gradually with increasing lag, with close agreement between observations and the TOMCAT CTM simulation after two to three months. Differences are largest at short lags, where the observational estimate shows stronger variability. The observations suggest that this link appears weaker during easterly QBO shear, linked to vertical ascent due to the strengthening of tropical upwelling (Baldwin et al., 2001). The total N_2O that emerges consistently O to O_3 effect (Fig. 7e) increases from lag zero to lag one (in the full 2004–2018 record and under both easterly and westerly shear regimes for this longer period. In the shorter subperiods, when masking data for the wind shear, this connection emerges during westerly wind shear in 2012–2018. This aligns with the understanding that westerly winds are linked to vertical descent due to the weakening of tropical upwelling (Baldwin et al., 2001). During the regime of the easterly wind shear, the causal discovery did not detect the connection from w^* to N_2O for the 2004–2011 and 2012–2018 periods, which is related to the very limited sample size. Further consistently detected connections across nearly all analyzed subperiods are the negative contemporaneous relationship from N_2O to period) and then gradually decreases toward longer lags. Here, observations also show a weaker total effect during easterly QBO phase. These results are also consistent with direct causal effects analyzed for different QBO regimes (see Fig. 6). The NO_2 , and from NO_2 to on O_3 . This aligns with the connections shown in Fig. 4a–c, highlighting the strong dependence and robustness of this chemical relationship across different regimes. Figure ?? further reveals regime-dependent differences in the causal links, particularly in the chemical connection from N effect (Fig. 7f) peaks at lag zero and rapidly decreases, approaching zero after about one month. This behavior is consistent with fast NO_x -driven O_3 chemistry. A slightly longer persistence during the earlier subperiod suggests a more sustained influence of NO_2 O to NO_2 . This link appears weaker during westerly shear, associated with reduced upwelling, and stronger during easterly shear, reflecting enhanced upwelling. Although the relatively short subperiods analyzed may influence the robustness of these results, Fig. ?? illustrates how causal discovery methods can capture both regime-specific and period-dependent interactions in stratospheric chemistry. on O_3 during that time.

5 Conclusions

This study applies causal inference to better understand quantify the contributions of chemical-dynamical drivers to that control O_3 variability in the tropical middle stratosphere. By using Using a causal discovery algorithm on observational data, we identify distinct causal relationships applied to observations over the 2004–2018 period, as well as within two key subperiods: 2004–2011 period, we robustly identify a dominant chemical–2011 and 2012–2018. The selection of these subperiods is motivated by contrasting dynamical pathway, in which variability in residual vertical velocity w^* modulates N_2O , subsequently affecting NO_2 and ultimately O_3 changes, namely declining levels in the first subperiod and increasing levels in the second. The resulting causal graphs show the capability are then used within the causal inference framework to quantify the temporal contribution of specific variables , namely w^* , N_2O , and NO_2 on monthly O_3 variability . Further, we used under different QBO phases and to separate the direct and mediated effects. In the TOMCAT CTM simulation, strong shared

variability among the chemical tracers limited the ability of the discovery algorithm to detect expected dynamical coupling. Therefore, we applied observational graphs based on triangulation (Uleman et al., 2024) to estimate causal relationships in the TOMCAT monthly data. This example illustrates a practical workaround for cases where models or datasets do not yield the expected causal structure through discovery. Importantly, estimating direct or total causal effects does not require that the graph be learned by an algorithm since a graph based on informed by expert knowledge and supported by the literature can serve as a valid alternative (Fons et al., 2023). In our case, the close agreement between the observationally derived graph and the main relationships anticipated from established chemical-dynamical interactions (see Fig. 4 and as discussed in the Introduction and shown in Fig. 4) demonstrates that the discovery algorithm can indeed recover the expected structure when applied to suitable data, highlighting its potential for uncovering causal connections even when they are not known a priori. Additionally, the toy model validation further demonstrates reliability under finite-sample conditions (Sect. 4.1). Therefore, the methodology adopted in this study, which integrates triangulation (Uleman et al., 2024) for the construction of causal graphs and an algorithm for causal effect estimation, demonstrates a comprehensive approach to causal inference. This ensures the robustness of the analyzed system and facilitates the quantification of specific connections in a physically meaningful domain.

In particular, the estimated direct and total causal connections yielded similar results for Direct causal effects applied to the observations and the TOMCAT CTM simulation. However, the connections involving residual vertical velocity w^* were somewhat stronger in the TOMCAT CTM simulation than in the observational data, especially beyond a lag of approximately one month. We found that a one-month lagged connection from N_2O to reveal that tropical middle-stratospheric O_3 variability is dominated by an indirect NO_2 during the 2012-mediated pathway, consistent with previous studies of chemical 2018 period robustly contrasted with the contemporaneous link observed during 2004–2011 and 2004–2018. This suggests that NO_2 production during 2012–2018 took longer, likely due to faster transport of N_2O and, consequently, its shorter residence time. Supporting this interpretation, the total causal effect across different time lags dynamical coupling (see Fig. 4 and e.g. Portmann et al., 2012). This mechanism of identified connections captures variability under different QBO phases via regime-oriented analysis and is also supported by sensitivity tests. For example, the direct influence of w^* on NO_2 , as well as w^* on O_3 (both mediated by N_2O) shows a one-month lagged influence during 2012–2018 compared to 2004–2011. This lagged influence is consequently seen in the direct effect of is weak and not robust across QBO phases. The total causal effects that consist of direct and mediated pathways peak at a lag of approximately two-three months (as discussed in Sect. 4.4, Fig. 7), indicating a propagation of the dynamical signal from w^* through N_2O on and NO_2 and the total effect of N_2O on O_3 . These differences in w^* - N_2O - NO_2 connections for the analyzed subperiods resulted in reduced NO_x formation during 2012–2018 and, consequently, lower catalytic O_3 destruction. It is important to emphasize that a deeper understanding of the physical mechanisms underlying the detected causal relationships is essential, especially when considering different dynamical regimes or processes. In this study, causal inference was applied separately to easterly and westerly wind shear regimes, revealing that the causal link from The process-oriented analysis for different QBO phases applied to the observations suggests that the chemical links between N_2O to and NO_2 was stronger during easterly shear than during westerly shear, and NO_2 and O_3 strengthen during westerly shear compared to easterly shear (see Fig. 6). Additional sensitivity tests, including temperature anomalies in the tropical middle stratosphere, did not yield a robust and interpretable graph. Temperature-related effects may therefore partly project

~~onto the identified NO₂-mediated pathway, but within the present framework their contribution cannot be robustly separated and quantified. However, the relatively short subperiods analyzed may affect the robustness of these findings and should be considered when interpreting the results.~~

590

Our study highlights the pivotal role causal inference can play in identifying, disentangling, and quantifying complex physical and chemical-dynamical processes in the stratosphere. This work lays the foundation for extending the application of causal inference to other areas ~~of stratospheric chemistry and stratospheric involving complex~~ chemical-dynamical interactions. Given its potential, this approach is particularly valuable for systems with connections that are not ~~yet fully understood.~~

595

~~Such an well understood. An~~ integration of causal reasoning into data-driven science ~~enhances will help us to enhance~~ our understanding of ~~processes and supports these complex processes and will support~~ the development of robust methodologies that combine machine learning with statistical approaches. This integration is especially relevant for Earth and environmental sciences, as it benefits both observational and modeling studies. Causal inference has already proven to be an effective tool for climate model evaluation, particularly by enabling comparisons between causal graphs derived from models and those based on observations. This emerging methodology is gaining traction in process-oriented climate model evaluation (Debeire et al., 2025; Karmouche et al., 2023; Galytska et al., 2023; Nowack et al., 2020) and offers valuable insights into the physical mechanisms driving the varying performance of different models. Notably, causal model evaluation not only identifies physically based connections but can also reveal the processes that are poorly represented in models. We also identify a key direction for future research focused on cross-evaluating the process-oriented performance of different CTMs and coupled chemistry-climate models (CCMs). Such efforts could provide valuable insights into model accuracy and reliability of CCMs, ensuring that the distribution of simulated species or processes is not driven by incorrect or unknown factors. Additionally, integrating causal inference with well-established statistical methods could further advance stratospheric studies, particularly in analyzing the variability of chemical species. Testing these approaches across different chemical and dynamical processes in various stratospheric regions represents a promising avenue for improving model evaluation and understanding complex interactions.

600

605

610 *Code and data availability.* The code used to reproduce results, including figures for this manuscript, will be accessible in Zenodo and in the following GitHub repository <https://github.com/EyringMLClimateGroup/>. The causal discovery algorithm is implemented in the Python package Tigramite is released under GNU General Public License v3.0. Tigramite v5 is publicly available on Zenodo <https://doi.org/10.5281/zenodo.6247837> Runge (2022) or via <https://github.com/jakobrunge/tigramite>, last access: 01.08.2025.

Transformed Eulerian mean data from the ERA5 reanalysis (monthly means) is available on Zenodo (<https://zenodo.org/records/7081721>, Serva, 2022). MLS N₂O v5.01 Lambert et al. (2020) is publicly available <https://disc.gsfc.nasa.gov/> upon registration. OSIRIS O₃ and NO₂ data are available at <https://research-groups.usask.ca/osiris/data-products.php#>. QBO equatorial winds are provided by the Institute of Meteorology and Climate Research at the Karlsruhe Institute of Technology (KIT) and are publicly available on Zenodo (<https://zenodo.org/records/18850668>, Kerzenmacher and Braesicke, 2026). Data from the TOMCAT CTM simulation is available upon request from the authors.

615

620 Appendix A: Stratospheric trends based on LOTUS regression model

To review the latitude–altitude changes in the distribution of analyzed species, we applied the open-source regression model Long-term Ozone Trends and Uncertainties in the Stratosphere (LOTUS, v0.8.3) (Godin-Beekmann et al., 2022). LOTUS employs the classical multiple linear regression method to estimate time series variability from proxies using the general least squares approach. In this study, we used the following proxies: QBO, ENSO, the 11-year solar cycle, stratospheric aerosol optical depth (sAOD), and a long-term trend. Independent linear trend (ILT) terms were introduced to assess changes in the analyzed species during 2004–2011 and 2012–2018. All data were monthly mean time series, deseasonalized within the LOTUS model using Fourier components to represent annual and semi-annual variations. The fitting of the deseasonalized time series followed the approach described by Godin-Beekmann et al. (2022), with the exception that QBO equatorial wind data from KIT was used and standardized at three vertical levels: 10, 30, and 50 hPa. Although the LOTUS model does not show statistically significant changes at the 90% confidence level for some species in certain subperiods, these intervals are retained to better understand the processes driving O_3 variability.

Latitude–altitude distribution of changes in (a-b) w^* in mm/s, (d-e) N_2O , (g-h) NO_2 , and (j-k) O_3 in % from the LOTUS regression model for two subperiods 2004–2011 and 2012–2018 and their corresponding vertical profiles in the tropical stratosphere in panels c,f,i,l. Hatched areas show changes that are not statistically significant at 90% confidence. The dashed boxes indicate the region of the tropical middle stratosphere.

Appendix A: Sensitivity tests

Choosing a τ_{max} that is too low risks missing causal links with longer delays, which violates the assumption of causal sufficiency. However, choosing τ_{max} too high without mitigation can dilute the detection power of the causal algorithm. Namely, a larger τ_{max} expands the search, as the algorithm tests more possible lagged pairs. This leads to larger conditioning sets, which can further reduce the effect size and detection power. Therefore, it is important to condition only on a few relevant variables that actually explain the relationship (Runge et al., 2019). Figures ?? and ?? demonstrate the results of the application of the causal discovery algorithm for observational datasets for the period 2004–2011 and 2012–2018 correspondingly with different setups of τ_{max} (depicted on the x-axis) and α_{pc} (depicted with markers). τ_{min} set to 0 to account for the contemporaneous connections. Sensitivity tests show very similar results based on different setups of τ_{max} and α_{pc} . During the 2011–2018 period, the link from N_2O to NO_2 is robustly detected as one month lagged, even with τ_{max} set to > 1 (??). The chemical connections from N_2O to NO_2 and from NO_2 to O_3 are robustly detected as contemporaneous across all experiments.

Sensitivity tests for the observed connections for the period 2004–2011 based on the application of the LPCMCI algorithm with different τ_{max} (1, 2, 3, 5, and 10) plotted on the x-axis and different α_{pc} (i.e. 0.01, 0.02, 0.05, 0.1, 0.2) depicted with markers. For all tests $\tau_{min} = 0$. Only the links discussed in Sect. 4.1 are shown.

650 Same as Fig. ?? but for the period 2012–2018.

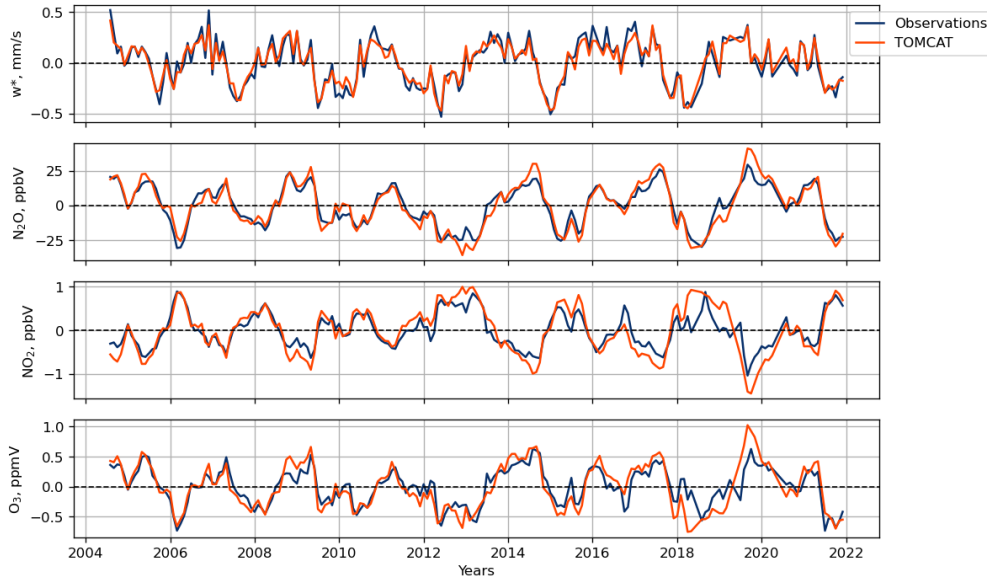


Figure A1. Monthly mean detrended anomalies over tropical middle stratosphere during ~~2004-2018~~ 2004-2021 in observations (blue) and the TOMCAT CTM simulation (orange). The TOMCAT CTM data is masked to match the occurrence of the observations.

Appendix A: Comparison of observations and the TOMCAT CTM simulation

The detrended monthly mean anomalies ~~over~~ in the tropical middle stratosphere from observations and the TOMCAT CTM simulation that were used for the causal inference are shown in Fig. A1. Monthly anomalies from the TOMCAT CTM simulation closely align with observations.

655 Figure A2 depicts lagged dependencies from observations (blue) and the TOMCAT CTM simulation (orange) in the tropical middle stratosphere during ~~2004-2018~~ 2004-2021 using the RobustParCorr class, i.e., computing lagged correlations after transforming all marginal distributions to Gaussians. Overall, the model reproduces both the sign and the magnitude of the observed relationships across most variable pairs and lags, with correlations generally decreasing in magnitude with increasing time lag. The autocorrelations of the analyzed variables are mostly similar between observations and the TOMCAT CTM simulation, except for $\text{NNO}_2\Theta$, which exhibits slightly ~~weaker~~ stronger autocorrelation in the TOMCAT CTM simulation across all time lags compared to observations. The ~~connection~~ connections between w^* and O_3 (first row, last column), N_2O and NO_2 and w^* and (second row, third column), and O_3 (top row, last two columns) is slightly ~~stronger~~ and NO_2 (last row, third column) also show stronger lagged dependencies in the TOMCAT CTM simulation in comparison to observations.

665 Figure A3 depicts kernel density estimates of the joint and marginal (diagonal panels) densities of w^* , N_2O , NO_2 , and O_3 in the tropical middle stratosphere. Color coding corresponds to Fig. A2. The contours illustrate the covariance structure between the variables, and the annotated τ values indicate the lag at which the strongest association is found. The overall orientation of

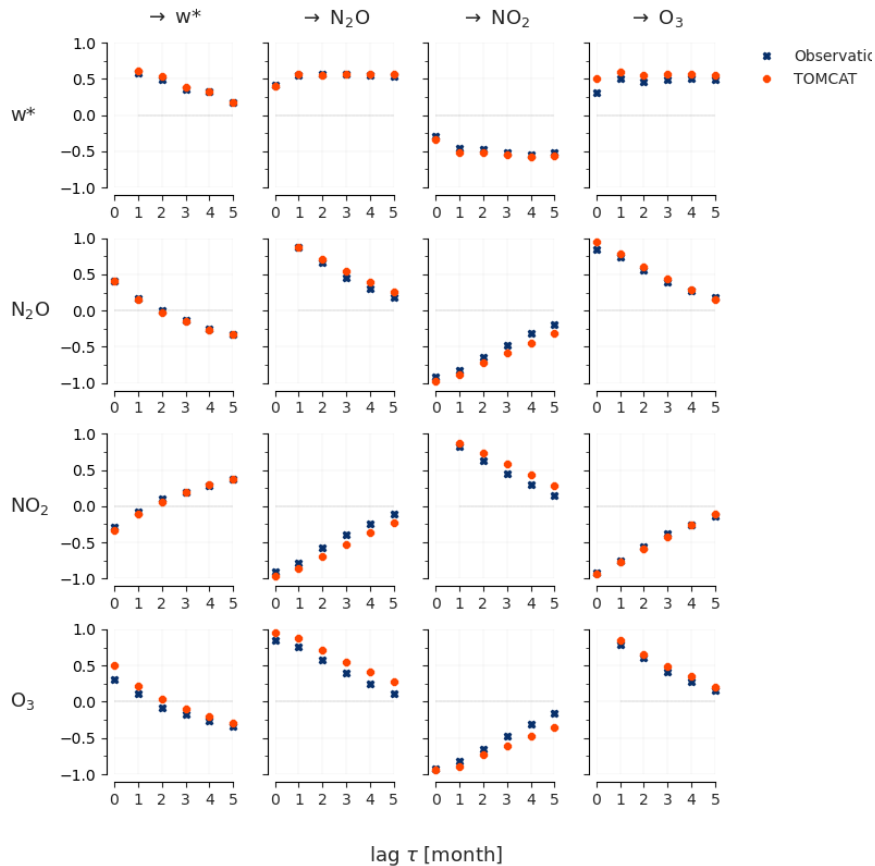


Figure A2. Lagged dependencies ~~over~~ in the tropical middle stratosphere during ~~2004-2018~~ 2004-2021 in observations (blue) and the TOMCAT CTM simulation (orange) based on the RobustParCorr class.

the contours is similar between observations and the TOMCAT CTM simulation, suggesting that the model captures the main sign of the relationships.

~~To further explore potential challenges in detecting anticipated causal graphs from the TOMCAT CTM simulation, we performed a set of sensitivity tests. Figure ?? illustrates the successful detection of anticipated connections (w^* - N_2O - NO_2 - O_3 chain) in observations (panel~~ It is important to highlight that the lagged dependencies (Fig. A2) and density plots (Fig. A3) only quantify pairwise co-variability. They do not separate direct from indirect effects and do not condition on other variables. Therefore, the lag at which the correlation is strongest should not be interpreted as the lag of a direct causal interaction. In a system with common dynamical forcing and persistence, pairwise correlations can reflect mixed pathways operating on different time scales.

Appendix B: Graphs inferred by the causal discovery algorithm and sensitivity testing

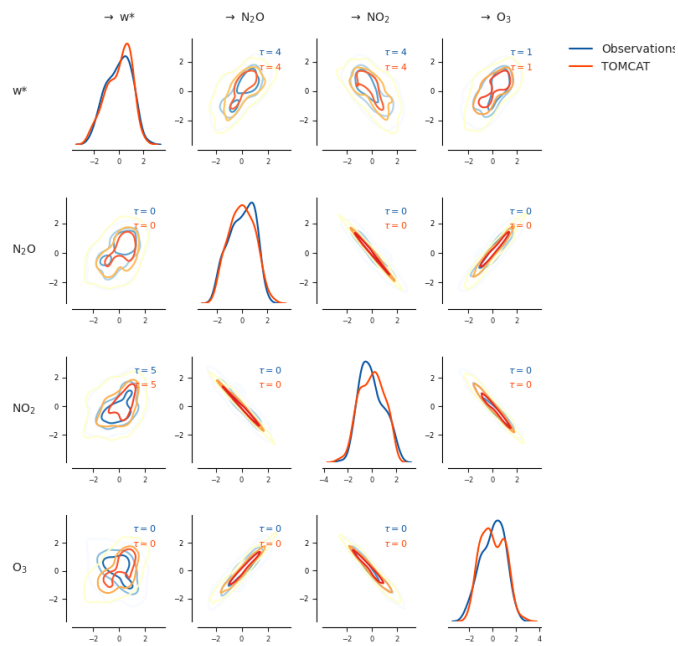


Figure A3. Density estimates of the joint and marginal densities over tropical middle stratosphere during 2004-2018-2004-2021 in observations (blue) and the TOMCAT CTM simulation (orange) based on the RobustParCorr class.

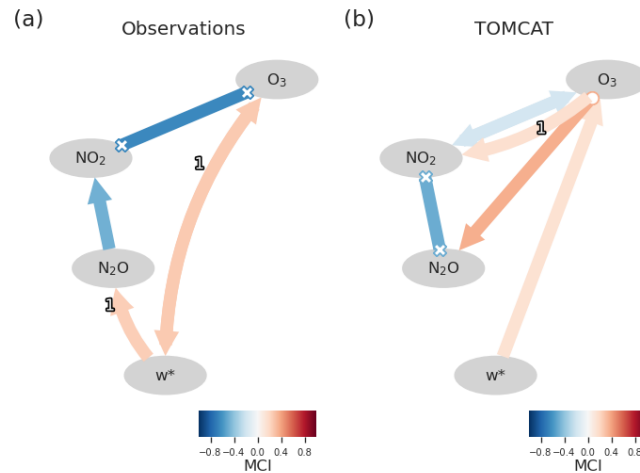


Figure B1. Causal graphs detected by the causal discovery algorithm from (a) observations (b) the TOMCAT CTM simulation for the period 2004-2021 with significance level $\alpha_{pc}=0.05$ and $\tau_{max}=2$.

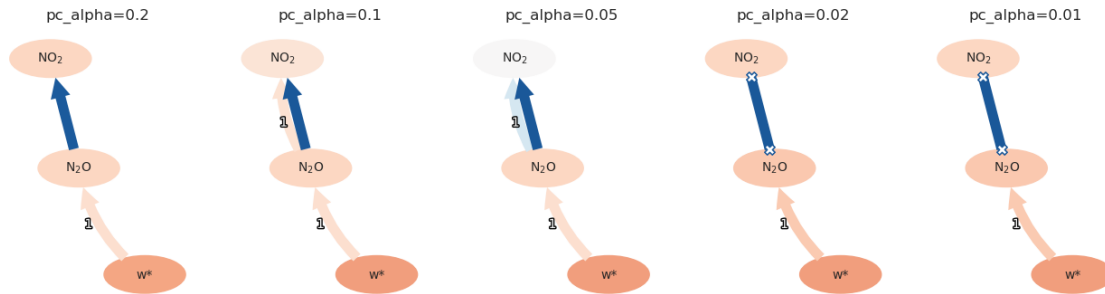


Figure B2. Causal graphs detected by the causal discovery algorithm from the TOMCAT CTM simulation for the period 2004-2021 with different significance level α_{pc} and $\tau_{max}=2$.

Figure B1 shows the causal graphs detected by the LPCMCI algorithm for the observations (a) and the ~~lack of detection of these connections in the~~ TOMCAT CTM simulation (panel b) in the tropical middle stratosphere during the period 2004-2018. b) for the period 2004-2021 with $\alpha_{pc} = 0.05$ and $\tau_{max} = 2$ in. For the observations, the causal discovery algorithm does not identify the direction of the N_2O - O_3 link. In addition, the w^* - O_3 connection is detected as bidirectional, indicating the presence of a latent common driver of w^* and O_3 rather than a resolved causal direction. For the TOMCAT CTM simulation, contrary to observations, the causal discovery algorithm does not detect the anticipated negative link from w^* to N_2O , however captures the negative contemporaneous links (without directions) between N_2O and NO_2 , and NO_2 and O_3 .

Further analysis of the output from the causal discovery ~~revealed that, in observations,~~ from the observations revealed that the algorithm successfully identified a significant lagged causal link from w^* to N_2O , indicating that past values of w^* have a direct influence on N_2O . This relationship remained significant even after conditioning on other variables and their lags, suggesting a robust causal connection. In contrast, in the TOMCAT CTM simulation, the same lagged link was initially detected but ~~was later removed after conditional independence testing. Specifically, after conditioning on~~ became statistically insignificant once O_3 was included in the conditioning set, indicating that O_3 at a lag of one month, the statistical dependence between w^* (lagged by one month) explains most of the shared variability between transport and N_2O (at the current time step) disappeared. This implies that, ~~To further investigate the reason for the removal of one-month lagged w^* to N_2O link in the TOMCAT CTM simulation, for the period 2004-2021, Fig. B2 shows the results of causal discovery after excluding O_3 at a one-month lag explains the relationship between~~ from the variable set. In this reduced setup, the w^* and N_2O , making the direct causal link from w^* to N_2O unnecessary. In this regard, we performed additional testing on the one-month lagged link reappeared and was statistically significant across tested α_{pc} . This indicates that the previously missing transport signal is not due to a lack of dynamical coupling in the TOMCAT CTM simulation and found that removing O_3 , but rather to conditional independence induced by the strong covariance among the chemical variables. In the TOMCAT CTM simulation, O_3 from the analyzed system and using the full dataset from 2004-2018 (without excluding dates where observational data was missing) allowed the causal discovery algorithm to detect the lagged connection between w^* and N_2O and has strong instantaneous coupling with both N_2O (see Fig. B2). In particular, as shown in Fig. B2, the lagged positive connection from w^* to N_2O and NO_2 , and therefore accounts

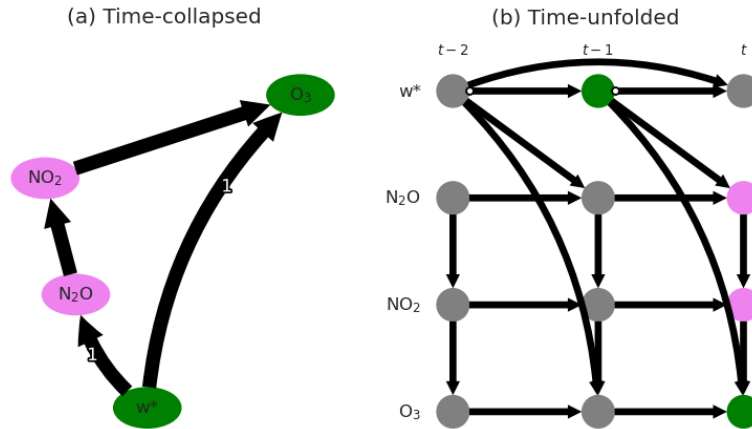


Figure C1. Example of the total effect of w^* on O_3 (green) as a sum of a direct lagged link and indirect via N_2O and NO_2 mediators (violet) in the time-collapsed graph (a) and time-unfolded graph (b), which corresponds to the causal graph from observations shown in Fig. 4a and time-unfolded graph (b).

for a large part of their common variability. Consequently, once conditioning on O_3 , the remaining unique contribution of w^* to N_2O simulation appears for the significance levels (α_{pc}) 0.2, 0.1, 0.05. This suggests that the absence of the causal link in TOMCAT may be sensitive to both the presence of variability is no longer statistically detectable. The re-emergence of the w^* to N_2O link in the reduced system (without O_3 in the model and data availability constraints-) therefore indicates that the transport influence is present, but in the full multivariate setup it becomes statistically hidden because the strongly coupled chemical tracers (O_3 and N_2O , and O_3 and NO_2) explain most of the same variability.

705

Causal graphs detected by the causal discovery algorithm from (a) observations (b) the TOMCAT CTM simulation for the period 2004-2018 with significance level $\alpha_{pc}=0.02$ and $\tau_{max}=1$.

Causal graphs detected by the causal discovery algorithm from the TOMCAT CTM simulation for the period 2004-2018 with different significance level α_{pc} and $\tau_{max}=1$.

710

Appendix C: Total causal effects

To better understand the causal effects across different time lags, Fig. C1 depicts (a) time-collapsed and (b) time-unfolded causal graphs based on the observational causal graph detected in Fig. 4b-a in the manuscript. As an example, the total effect of w^* on O_3 (green nodes) consists of a direct path from w^* to O_3 and an indirect path, which is mediated by N_2O and NO_2 (violet nodes) as shown in Fig. C1a. The indirect path of the influence of w^* on O_3 is then better represented via a time series causal graph (Fig. C1b). The total causal effect across different time lags of this relationship is shown and discussed in Fig. 7c in the manuscript.

715

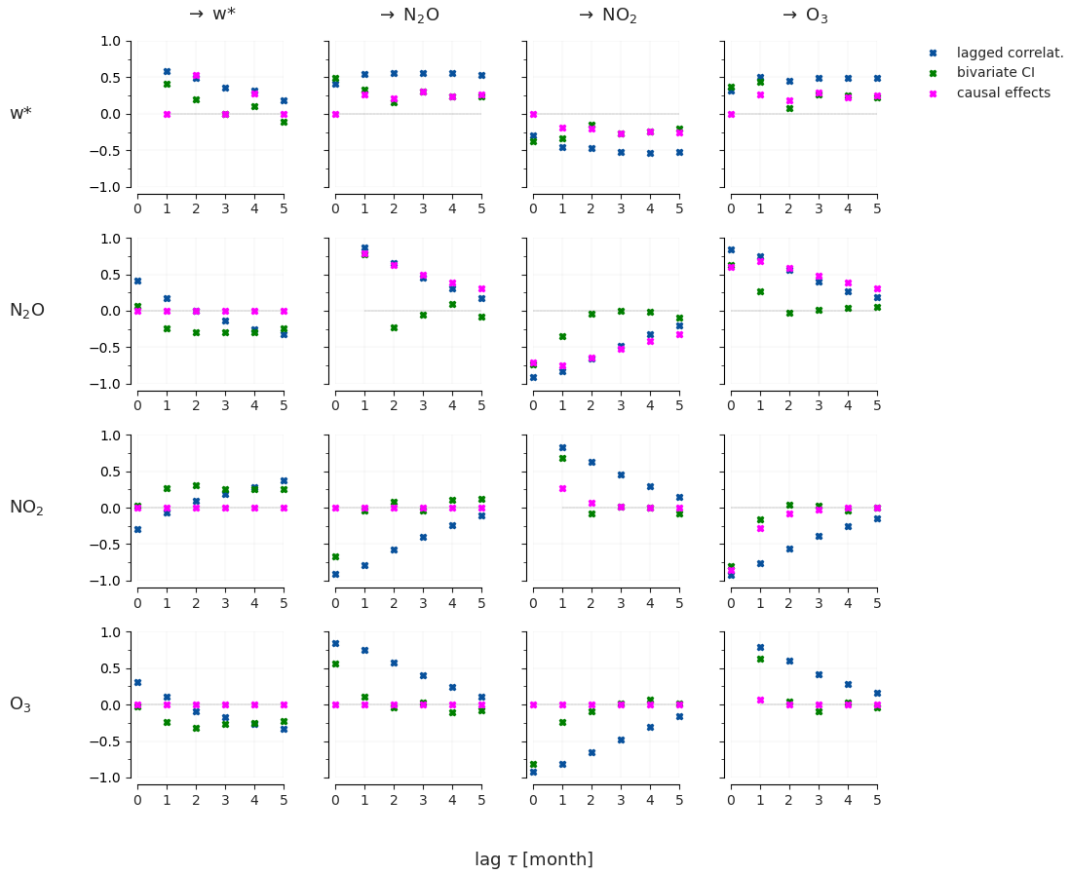


Figure D1. Lagged dependencies across different time lags (in months) from observations for the period 2004-2018-2004-2021 based on partial correlations (blue), bivariate partial correlations (green), and estimated Wright coefficients (magenta).

Appendix D: Dependencies vs. causal effects across different time lags

720 The lagged unconditional dependencies, such as the lagged correlations based on partial correlation, are helpful to identify the maximal time lag τ_{max} to choose in the causal discovery algorithm. However, large autocorrelation might inflate lag peaks Runge et al. (2014). To condition out some part of the autocorrelation, the bivariate, lagged CI test (partial correlation as an example) can be applied. The comparison between the lagged dependencies from both tests is shown in Fig. D1. We also plot lagged dependencies based on the calculated Wright coefficient (labeled as 'causal effects'), which directly indicates the strength of causal relationships and takes into account the direction of causal influence (see, e.g. Fig. 4 in the manuscript). For 725 example, the causal effects in the last row in Fig. D1 are all zero since O_3 is not a cause of any analyzed variable in the system.

Author contributions. E.G. performed the analysis, prepared all figures, and led the writing of the manuscript. J.R. developed the causal discovery tool that supported this study. E.G. developed the code for data pre- and post-processing and implemented a causal inference workflow using J.R.’s package and code from Fons et al. (2023). M.P.C., S.S.D., and W.F. designed and performed the TOMCAT CTM simulation. All co-authors commented on the initial and revised drafts of the manuscripts and contributed to the interpretation of the results.

730 *Competing interests.* The authors declare no financial or non-financial competing interests

Acknowledgements. This research was funded by the Central Research Development Fund at the University of Bremen, Funding No: ZF04A/2023/FB1/Galytska Evgenia. Part of the funding for this study was provided by the European Research Council (ERC) Synergy Grant “Understanding and Modelling the Earth System with Machine Learning (USMILE)” under the Horizon 2020 research and innovation programme (Grant agreement 855187), the European Union’s Horizon 2020 research and innovation programme under Grant Agreement 101003536 (ESM2025—Earth System Models for the Future), and the “Advanced Earth System Model Evaluation for CMIP (EVal4CMIP)” project funded by the Helmholtz Society. J.R. has received funding from the European Research Council (ERC) Starting Grant CausalEarth under the European Union’s Horizon 2020 research and innovation program (Grant Agreement No. 948112). ~~The TOMCAT modelling was supported by NERC grant M.P.C. and S.S.D. are supported by the NCEO TerraFIRMA, NERC LSO3 (NE/V011863/1-1) and ESA OREGANO (4000137112/22/I-AG) projects.~~ This work used the computational resources of the Deutsches Klimarechenzentrum (DKRZ, 740 Germany) granted by its Scientific Steering Committee (WLA) under project ID bd1083. The authors thank Veronika Eyring for her comments on the study. The authors thank the Swedish National Space Agency and the Canadian Space Agency for the continued operation and support of Odin-OSIRIS.

References

- Abalos, M., Legras, B., Ploeger, F., and Randel, W. J.: Evaluating the advective Brewer-Dobson circulation in three reanalyses for the period
745 1979–2012, *Journal of Geophysical Research: Atmospheres*, 120, 7534–7554, <https://doi.org/10.1002/2015JD023182>, 2015.
- Arosio, C., Rozanov, A., Malinina, E., Eichmann, K.-U., von Clarmann, T., and Burrows, J. P.: Retrieval of ozone profiles from OMPS limb
scattering observations, *Atmospheric Measurement Techniques*, 11, 2135–2149, <https://doi.org/10.5194/amt-11-2135-2018>, 2018.
- Arosio, C., Rozanov, A., Malinina, E., Weber, M., and Burrows, J. P.: Merging of ozone profiles from SCIAMACHY, OMPS and SAGE II
750 observations to study stratospheric ozone changes, *Atmospheric Measurement Techniques*, 12, 2423–2444, <https://doi.org/10.5194/amt-12-2423-2019>, 2019.
- Arosio, C., Chipperfield, M. P., Rozanov, A., Weber, M., Dhomse, S., Feng, W., Jaross, G., Zhou, X., and Burrows, J. P.: Investigating Zonal
Asymmetries in Stratospheric Ozone Trends From Satellite Limb Observations and a Chemical Transport Model, *Journal of Geophysical
Research: Atmospheres*, 129, e2023JD040 353, <https://doi.org/10.1029/2023JD040353>, 2024.
- Baldwin, M. P., Gray, L. J., Dunkerton, T. J., Hamilton, K., Haynes, P. H., Randel, W. J., Holton, J. R., Alexander, M. J., Hirota, I., Horinouchi,
755 T., Jones, D. B. A., Kinnerson, J. S., Marquardt, C., Sato, K., and Takahashi, M.: The quasi-biennial oscillation, *Reviews of Geophysics*,
39, 179–229, <https://doi.org/10.1029/1999RG000073>, 2001.
- Ball, W. T., Alsing, J., Mortlock, D. J., Staehelin, J., Haigh, J. D., Peter, T., Tummon, F., Stübi, R., Stenke, A., Anderson, J., Bourassa, A.,
Davis, S. M., Degenstein, D., Frith, S., Froidevaux, L., Roth, C., Sofieva, V., Wang, R., Wild, J., Yu, P., Ziemke, J. R., and Rozanov, E. V.:
Evidence for a continuous decline in lower stratospheric ozone offsetting ozone layer recovery, *Atmospheric Chemistry and Physics*, 18,
760 1379–1394, <https://doi.org/10.5194/acp-18-1379-2018>, 2018.
- Blyth, C. R.: On Simpson’s Paradox and the Sure-Thing Principle, *Journal of the American Statistical Association*, 67, 364–366,
<https://doi.org/10.1080/01621459.1972.10482387>, 1972.
- Bognar, K., Tegtmeier, S., Bourassa, A., Roth, C., Warnock, T., Zawada, D., and Degenstein, D.: Stratospheric ozone trends for 1984–2021 in
the SAGE II–OSIRIS–SAGE III/ISS composite dataset, *Atmospheric Chemistry and Physics*, 22, 9553–9569, <https://doi.org/10.5194/acp-22-9553-2022>, 2022.
- Bönisch, H., Engel, A., Birner, T., Hoor, P., Tarasick, D. W., and Ray, E. A.: On the structural changes in the Brewer-Dobson circulation after
2000, *Atmospheric Chemistry and Physics*, 11, 3937–3948, <https://doi.org/10.5194/acp-11-3937-2011>, 2011.
- Bourassa, A. E., Roth, C. Z., Zawada, D. J., Rieger, L. A., McLinden, C. A., and Degenstein, D. A.: Drift-corrected Odin-OSIRIS ozone prod-
uct: algorithm and updated stratospheric ozone trends, *Atmospheric Measurement Techniques*, 11, 489–498, <https://doi.org/10.5194/amt-11-489-2018>, 2018.
- Camps-Valls, G., Gerhardus, A., Ninad, U., Varando, G., Martius, G., Balaguer-Ballester, E., Vinuesa, R., Diaz, E., Zanna, L., and Runge,
J.: Discovering causal relations and equations from data, *Physics Reports*, 1044, 1–68, <https://doi.org/10.1016/j.physrep.2023.10.005>,
discovering causal relations and equations from data, 2023.
- Carvalho-Oliveira, J., Di Capua, G., Borchert, L. F., Donner, R. V., and Baehr, J.: Causal relationships and predictability of the summer East
775 Atlantic teleconnection, *Weather and Climate Dynamics*, 5, 1561–1578, <https://doi.org/10.5194/wcd-5-1561-2024>, 2024.
- Chapman, S.: XXXV. On ozone and atomic oxygen in the upper atmosphere, *The London, Edinburgh, and Dublin Philosophical Magazine
and Journal of Science*, 10, 369–383, <https://doi.org/10.1080/14786443009461588>, 1930.
- Chipperfield, M. P.: New version of the TOMCAT/SLIMCAT off-line chemical transport model: Intercomparison of stratospheric tracer
experiments, *Quarterly Journal of the Royal Meteorological Society*, 132, 1179–1203, <https://doi.org/10.1256/qj.05.51>, 2006.

- 780 Chipperfield, M. P. and Bekki, S.: Opinion: Stratospheric ozone – depletion, recovery and new challenges, *Atmospheric Chemistry and Physics*, 24, 2783–2802, <https://doi.org/10.5194/acp-24-2783-2024>, 2024.
- Chipperfield, M. P. and Gray, L. J.: Two-dimensional model studies of the interannual variability of trace gases in the middle atmosphere, *Journal of Geophysical Research: Atmospheres*, 97, 5963–5980, <https://doi.org/10.1029/92JD00029>, 1992.
- Chipperfield, M. P., Gray, L. J., Kinnersley, J. S., and Zawodny, J.: A Two-Dimensional Model Study of the QBO Signal in SAGE II NO₂
785 and O₃, *Geophysical Research Letters*, 21, 589–592, <https://doi.org/10.1029/94GL00211>, 1994.
- Chipperfield, M. P., Liang, Q., Strahan, S. E., Morgenstern, O., Dhomse, S. S., Abraham, N. L., Archibald, A. T., Bekki, S., Braesicke, P., Di Genova, G., Fleming, E. L., Hardiman, S. C., Iachetti, D., Jackman, C. H., Kinnison, D. E., Marchand, M., Pitari, G., Pyle, J. A., Rozanov, E., Stenke, A., and Tummon, F.: Multimodel estimates of atmospheric lifetimes of long-lived ozone-depleting substances: Present and future, *Journal of Geophysical Research: Atmospheres*, 119, 2555–2573, <https://doi.org/10.1002/2013JD021097>, 2014.
- 790 Chrysanthou, A., Dubé, K., Tegtmeier, S., and Chipperfield, M. P.: Hemispheric Asymmetry in Stratospheric Trends of HCl and Ozone: Impact of Chemical Feedback on Ozone Recovery, *Journal of Geophysical Research: Atmospheres*, 130, e2024JD042161, <https://doi.org/10.1029/2024JD042161>, e2024JD042161 2024JD042161, 2025.
- Crutzen, P. J.: The influence of nitrogen oxides on the atmospheric ozone content, *Quarterly Journal of the Royal Meteorological Society*, 96, 320–325, <https://doi.org/10.1002/qj.49709640815>, 1970.
- 795 Davis, S. M., Rosenlof, K. H., Hassler, B., Hurst, D. F., Read, W. G., Vömel, H., Selkirk, H., Fujiwara, M., and Damadeo, R.: The Stratospheric Water and Ozone Satellite Homogenized (SWOOSH) database: a long-term database for climate studies, *Earth System Science Data*, 8, 461–490, <https://doi.org/10.5194/essd-8-461-2016>, 2016.
- Debeire, K., Bock, L., Nowack, P., Runge, J., and Eyring, V.: Constraining uncertainty in projected precipitation over land with causal discovery, *Earth System Dynamics*, 16, 607–630, <https://doi.org/10.5194/esd-16-607-2025>, 2025.
- 800 Denzin, N. K.: *The Fundamentals: Introducing Triangulation*, <https://www.shortcutstv.com/wp-content/uploads/2021/01/Introducing-Triangulation.pdf>, 2010.
- Dhomse, S. S., Chipperfield, M. P., Feng, W., Hossaini, R., Mann, G. W., and Santee, M. L.: Revisiting the hemispheric asymmetry in midlatitude ozone changes following the Mount Pinatubo eruption: A 3-D model study, *Geophysical Research Letters*, 42, 3038–3047, <https://doi.org/https://doi.org/10.1002/2015GL063052>, 2015.
- 805 Dhomse, S. S., Chipperfield, M. P., Damadeo, R. P., Zawodny, J. M., Ball, W. T., Feng, W., Hossaini, R., Mann, G. W., and Haigh, J. D.: On the ambiguous nature of the 11 year solar cycle signal in upper stratospheric ozone, *Geophysical Research Letters*, 43, 7241–7249, <https://doi.org/https://doi.org/10.1002/2016GL069958>, 2016.
- Dhomse, S. S., Kinnison, D., Chipperfield, M. P., Salawitch, R. J., Cionni, I., Hegglin, M. I., Abraham, N. L., Akiyoshi, H., Archibald, A. T., Bednarz, E. M., Bekki, S., Braesicke, P., Butchart, N., Dameris, M., Deushi, M., Frith, S., Hardiman, S. C., Hassler, B., Horowitz, L. W.,
810 Hu, R.-M., Jöckel, P., Josse, B., Kirner, O., Kremser, S., Langematz, U., Lewis, J., Marchand, M., Lin, M., Mancini, E., Marécal, V., Michou, M., Morgenstern, O., O’Connor, F. M., Oman, L., Pitari, G., Plummer, D. A., Pyle, J. A., Revell, L. E., Rozanov, E., Schofield, R., Stenke, A., Stone, K., Sudo, K., Tilmes, S., Visionsi, D., Yamashita, Y., and Zeng, G.: Estimates of ozone return dates from Chemistry-Climate Model Initiative simulations, *Atmospheric Chemistry and Physics*, 18, 8409–8438, <https://doi.org/10.5194/acp-18-8409-2018>, 2018.
- 815 Docquier, D., Vannitsem, S., Ragone, F., Wyser, K., and Liang, X. S.: Causal Links Between Arctic Sea Ice and Its Potential Drivers Based on the Rate of Information Transfer, *Geophysical Research Letters*, 49, e2021GL095892, <https://doi.org/10.1029/2021GL095892>, 2022.

- Dubé, K., Zawada, D., Bourassa, A., Degenstein, D., Randel, W., Flittner, D., Sheese, P., and Walker, K.: An improved OSIRIS NO₂ profile retrieval in the upper troposphere–lower stratosphere and intercomparison with ACE-FTS and SAGE III/ISS, *Atmospheric Measurement Techniques*, 15, 6163–6180, <https://doi.org/10.5194/amt-15-6163-2022>, 2022.
- 820 Dubé, K., Randel, W., Bourassa, A., Zawada, D., McLinden, C., and Degenstein, D.: Trends and Variability in Stratospheric NO_x Derived From Merged SAGE II and OSIRIS Satellite Observations, *Journal of Geophysical Research: Atmospheres*, 125, e2019JD031798, <https://doi.org/10.1029/2019JD031798>, 2020.
- Eckert, E., von Clarmann, T., Kiefer, M., Stiller, G. P., Lossow, S., Glatthor, N., Degenstein, D. A., Froidevaux, L., Godin-Beekmann, S., Leblanc, T., McDermid, S., Pastel, M., Steinbrecht, W., Swart, D. P. J., Walker, K. A., and Bernath, P. F.: Drift-corrected trends and periodic
825 variations in MIPAS IMK/IAA ozone measurements, *Atmospheric Chemistry and Physics*, 14, 2571–2589, <https://doi.org/10.5194/acp-14-2571-2014>, 2014.
- Eyring, V., Cionni, I., Bodeker, G. E., Charlton-Perez, A. J., Kinnison, D. E., Scinocca, J. F., Waugh, D. W., Akiyoshi, H., Bekki, S., Chipperfield, M. P., Dameris, M., Dhomse, S., Frith, S. M., Garny, H., Gettelman, A., Kubin, A., Langematz, U., Mancini, E., Marchand, M., Nakamura, T., Oman, L. D., Pawson, S., Pitari, G., Plummer, D. A., Rozanov, E., Shepherd, T. G., Shibata, K., Tian, W.,
830 Braesicke, P., Hardiman, S. C., Lamarque, J. F., Morgenstern, O., Pyle, J. A., Smale, D., and Yamashita, Y.: Multi-model assessment of stratospheric ozone return dates and ozone recovery in CCMVal-2 models, *Atmospheric Chemistry and Physics*, 10, 9451–9472, <https://doi.org/10.5194/acp-10-9451-2010>, 2010.
- Eyring, V., Collins, W. D., Gentine, P., Barnes, E. A., Barreiro, M., Beucler, T., Bocquet, M., Bretherton, C. S., Christensen, H. M., Dagon, K., et al.: Pushing the frontiers in climate modelling and analysis with machine learning, *Nature Climate Change*, 14, 916–928,
835 <https://doi.org/10.1038/s41558-024-02095-y>, 2024.
- Fons, E., Runge, J., Neubauer, D., and Lohmann, U.: Stratocumulus adjustments to aerosol perturbations disentangled with a causal approach, *npj Climate and Atmospheric Science*, 6, 130, <https://doi.org/10.1038/s41612-023-00452-w>, 2023.
- Galytska, E.: Spatio-temporal variations of observed and modelled stratospheric trace gases, Ph.D. thesis, Universität Bremen, <https://nbn-resolving.de/urn:nbn:de:gbv:46-00107599-10>, 2019.
- 840 Galytska, E., Rozanov, A., Chipperfield, M. P., Dhomse, Weber, M., Arosio, C., Feng, W., and Burrows, J. P.: Dynamically controlled ozone decline in the tropical mid-stratosphere observed by SCIAMACHY, *Atmospheric Chemistry and Physics*, 19, 767–783, <https://doi.org/10.5194/acp-19-767-2019>, 2019.
- Galytska, E., Weigel, K., Handorf, D., Jaiser, R., Köhler, R., Runge, J., and Eyring, V.: Evaluating Causal Arctic-Midlatitude Teleconnections in CMIP6, *Journal of Geophysical Research: Atmospheres*, 128, e2022JD037978, <https://doi.org/10.1029/2022JD037978>, 2023.
- 845 Gebhardt, C., Rozanov, A., Hommel, R., Weber, M., Bovensmann, H., Burrows, J. P., Degenstein, D., Froidevaux, L., and Thompson, A. M.: Stratospheric ozone trends and variability as seen by SCIAMACHY from 2002 to 2012, *Atmospheric Chemistry and Physics*, 14, 831–846, <https://doi.org/10.5194/acp-14-831-2014>, 2014.
- Gerhardus, A. and Runge, J.: High-recall causal discovery for autocorrelated time series with latent confounders, in: *Advances in Neural Information Processing Systems*, edited by Larochelle, H., Ranzato, M., Hadsell, R., Balcan, M., and Lin, H., vol. 33, pp. 12615–
850 12625, Curran Associates, Inc., https://proceedings.neurips.cc/paper_files/paper/2020/file/94e70705efae423efda1088614128d0b-Paper.pdf, 2020.
- Godin-Beekmann, S., Azouz, N., Sofieva, V. F., Hubert, D., Petropavlovskikh, I., Effertz, P., Ancellet, G., Degenstein, D. A., Zawada, D., Froidevaux, L., Frith, S., Wild, J., Davis, S., Steinbrecht, W., Leblanc, T., Querel, R., Tourpali, K., Damadeo, R., Maillard Barras, E., Stübi, R., Vigouroux, C., Arosio, C., Nedoluha, G., Boyd, I., Van Malderen, R., Mahieu, E., Smale, D., and Sussmann, R.: Updated trends

- 855 of the stratospheric ozone vertical distribution in the 60° S–60° N latitude range based on the LOTUS regression model, *Atmospheric Chemistry and Physics*, 22, 11 657–11 673, <https://doi.org/10.5194/acp-22-11657-2022>, 2022.
- Hersbach, H., Bell, B., Berrisford, P., Hirahara, S., Horányi, A., Muñoz-Sabater, J., Nicolas, J., Peubey, C., Radu, R., Schepers, D., Simmons, A., Soci, C., Abdalla, S., Abellan, X., Balsamo, G., Bechtold, P., Biavati, G., Bidlot, J., Bonavita, M., De Chiara, G., Dahlgren, P., Dee, D., Diamantakis, M., Dragani, R., Flemming, J., Forbes, R., Fuentes, M., Geer, A., Haimberger, L., Healy, S., Hogan, R. J.,
860 Hólm, E., Janisková, M., Keeley, S., Lalouaux, P., Lopez, P., Lupu, C., Radnoti, G., de Rosnay, P., Rozum, I., Vamborg, F., Villaume, S., and Thépaut, J.-N.: The ERA5 global reanalysis, *Quarterly Journal of the Royal Meteorological Society*, 146, 1999–2049, <https://doi.org/10.1002/qj.3803>, 2020.
- Iglesias-Suarez, F., Wild, O., Kinnison, D. E., Garcia, R. R., Marsh, D. R., Lamarque, J.-F., Ryan, E. M., Davis, S. M., Eichinger, R., Saiz-Lopez, A., and Young, P. J.: Tropical Stratospheric Circulation and Ozone Coupled to Pacific Multi-Decadal Variability, *Geophysical Research Letters*, 48, e2020GL092 162, <https://doi.org/10.1029/2020GL092162>, 2021.
865
- Karmouche, S., Galytska, E., Runge, J., Meehl, G. A., Phillips, A. S., Weigel, K., and Eyring, V.: Regime-oriented causal model evaluation of Atlantic–Pacific teleconnections in CMIP6, *Earth System Dynamics*, 14, 309–344, <https://doi.org/10.5194/esd-14-309-2023>, 2023.
- Kerzenmacher, T. and Braesicke, P.: QBO: monthly zonal stratospheric winds from tropical radiosonde data (mainly Singapore), <https://doi.org/10.5281/zenodo.18472673>, 2026.
- 870 Kretschmer, M., Zappa, G., and Shepherd, T. G.: The role of Barents–Kara sea ice loss in projected polar vortex changes, *Weather and Climate Dynamics*, 1, 715–730, <https://doi.org/10.5194/wcd-1-715-2020>, 2020.
- Krich, C., Runge, J., Miralles, D. G., Migliavacca, M., Perez-Priego, O., El-Madany, T., Carrara, A., and Mahecha, M. D.: Estimating causal networks in biosphere–atmosphere interaction with the PCMCi approach, *Biogeosciences*, 17, 1033–1061, <https://doi.org/10.5194/bg-17-1033-2020>, 2020.
- 875 Kuttippurath, J., Gopikrishnan, G. P., Müller, R., Godin-Beekmann, S., and Brioude, J.: No severe ozone depletion in the tropical stratosphere in recent decades, *Atmospheric Chemistry and Physics*, 24, 6743–6756, <https://doi.org/10.5194/acp-24-6743-2024>, 2024.
- Kyrölä, E., Laine, M., Sofieva, V., Tamminen, J., Päivärinta, S.-M., Tukiainen, S., Zawodny, J., and Thomason, L.: Combined SAGE II–GOMOS ozone profile data set for 1984–2011 and trend analysis of the vertical distribution of ozone, *Atmospheric Chemistry and Physics*, 13, 10 645–10 658, <https://doi.org/10.5194/acp-13-10645-2013>, 2013.
- 880 Lambert, A., Livesey, N., Read, W., and Fuller, R.: MLS/Aura Level 3 Monthly Binned Nitrous Oxide (N₂O) Mixing Ratio on Assorted Grids V005, https://disc.gsfc.nasa.gov/datasets/ML2N2O_003/summary, <https://doi.org/10.5067/Aura/MLS/DATA/3545>, accessed: [05.03.2025], 2020.
- Li, Y., Dhomse, S. S., Chipperfield, M. P., Feng, W., Bian, J., Xia, Y., and Guo, D.: Quantifying stratospheric ozone trends over 1984–2020: a comparison of ordinary and regularized multivariate regression models, *Atmospheric Chemistry and Physics*, 23, 13 029–13 047,
885 <https://doi.org/10.5194/acp-23-13029-2023>, 2023.
- Llewellyn, E. J., Lloyd, N. D., Degenstein, D. A., Gattinger, R. L., Petelina, S. V., Bourassa, A. E., Wiensz, J. T., Ivanov, E. V., McDade, I. C., Solheim, B. H., McConnell, J. C., Haley, C. S., von Savigny, C., Sioris, C. E., McLinden, C. A., Griffioen, E., Kaminski, J., Evans, W. F., Puckrin, E., Strong, K., Wehrle, V., Hum, R. H., Kendall, D. J., Matsushita, J., Murtagh, D. P., Brohede, S., Stegman, J., Witt, G., Barnes, G., Payne, W. F., Piché, L., Smith, K., Warshaw, G., Deslauniers, D. L., Marchand, P., Richardson, E. H., King, R. A., Wevers, I., McCreath, W., Kyrölä, E., Oikarinen, L., Leppelmeier, G. W., Auvinen, H., Mégie, G., Hauchecorne, A., Lefèvre, F., de La Nöe, J.,
890 Ricaud, P., Frisk, U., Sjöberg, F., von Schéele, F., and Nordh, L.: The OSIRIS instrument on the Odin spacecraft, *Canadian Journal of Physics*, 82, 411–422, <https://doi.org/10.1139/p04-005>, 2004.

- Match, A. and Fueglistaler, S.: Anomalous Dynamics of QBO Disruptions Explained by 1D Theory with External Triggering, *Journal of the Atmospheric Sciences*, 78, 373 – 383, <https://doi.org/10.1175/JAS-D-20-0172.1>, 2021.
- 895 Ming, A., Hitchcock, P., Orbe, C., and Dubé, K.: Phase and Amplitude Relationships Between Ozone, Temperature, and Circulation in the Quasi-Biennial Oscillation, *Journal of Geophysical Research: Atmospheres*, 130, e2024JD042469, <https://doi.org/https://doi.org/10.1029/2024JD042469>, e2024JD042469 2024JD042469, 2025.
- Minganti, D., Chabrilat, S., Christophe, Y., Errera, Q., Abalos, M., Prignon, M., Kinnison, D. E., and Mahieu, E.: Climatological impact of the Brewer–Dobson circulation on the N_2O budget in WACCM, a chemical reanalysis and a CTM driven by four dynamical reanalyses, *Atmospheric Chemistry and Physics*, 20, 12 609–12 631, <https://doi.org/10.5194/acp-20-12609-2020>, 2020.
- 900 Murtagh, D., Frisk, U., Merino, F., Ridal, M., Jonsson, A., Stegman, J., Witt, G., Eriksson, P., Jiménez, C., Megie, G., Noë, J. d. l., Ricaud, P., Baron, P., Pardo, J. R., Hauchcorne, A., Llewellyn, E. J., Degenstein, D. A., Gattinger, R. L., Lloyd, N. D., Evans, W. F., McDade, I. C., Haley, C. S., Sioris, C., Savigny, C. v., Solheim, B. H., McConnell, J. C., Strong, K., Richardson, E. H., Leppelmeier, G. W., Kyrölä, E., Auvinen, H., and Oikarinen, L.: An overview of the Odin atmospheric mission, *Canadian Journal of Physics*, 80, 309–319, <https://doi.org/10.1139/p01-157>, 2002.
- 905 Nedoluha, G. E., Siskind, D. E., Lambert, A., and Boone, C.: The decrease in mid-stratospheric tropical ozone since 1991, *Atmospheric Chemistry and Physics*, 15, 4215–4224, <https://doi.org/10.5194/acp-15-4215-2015>, 2015.
- Nisbet, E. G., Dlugokencky, E. J., Fisher, R. E., France, J. L., Lowry, D., Manning, M. R., Michel, S. E., and Warwick, N. J.: Atmospheric methane and nitrous oxide: challenges along the path to Net Zero, *Philosophical Transactions of the Royal Society A: Mathematical, Physical and Engineering Sciences*, 379, 20200457, <https://doi.org/10.1098/rsta.2020.0457>, 2021.
- 910 Nowack, P., Runge, J., Eyring, V., and Haigh, J. D.: Causal networks for climate model evaluation and constrained projections, *Nature communications*, 11, 1–11, <https://doi.org/10.1038/s41467-020-15195-y>, 2020.
- Park, M., Randel, W. J., Kinnison, D. E., Bourassa, A. E., Degenstein, D. A., Roth, C. Z., McLinden, C. A., Sioris, C. E., Livesey, N. J., and Santee, M. L.: Variability of Stratospheric Reactive Nitrogen and Ozone Related to the QBO, *Journal of Geophysical Research: Atmospheres*, 122, 10,103–10,118, <https://doi.org/10.1002/2017JD027061>, 2017.
- 915 Petropavlovskikh, I., Godin-Beekmann, S., Hubert, D., Damadeo, R., Hassler, B., and Sofieva, V.: SPARC/IO3C/GAW Report on Long-term Ozone Trends and Uncertainties in the Stratosphere, Tech. rep., <https://doi.org/10.17874/f899e57a20b>, 9th assessment report of the SPARC project, published by the International Project Office at DLR-IPA. also: GAW Report No. 241; WCRP Report 17/2018, 2019.
- Polkova, I., Afargan-Gerstman, H., Domeisen, D. I. V., King, M. P., Ruggieri, P., Athanasiadis, P., Dobrynin, M., Aarnes, , Kretschmer, M., and Baehr, J.: Predictors and prediction skill for marine cold-air outbreaks over the Barents Sea, *Quarterly Journal of the Royal Meteorological Society*, 147, 2638–2656, <https://doi.org/10.1002/qj.4038>, 2021.
- 920 Portmann, R. W., Daniel, J. S., and Ravishankara, A. R.: Stratospheric ozone depletion due to nitrous oxide: influences of other gases, *Philosophical Transactions of the Royal Society B: Biological Sciences*, 367, 1256–1264, <https://doi.org/10.1098/rstb.2011.0377>, 2012.
- Prather, M. J., Froidevaux, L., and Livesey, N. J.: Observed changes in stratospheric circulation: decreasing lifetime of N_2O , 2005–2021, *Atmospheric Chemistry and Physics*, 23, 843–849, <https://doi.org/10.5194/acp-23-843-2023>, 2023.
- 925 Ravishankara, A. R., Daniel, J. S., and Portmann, R. W.: Nitrous Oxide (N_2O): The Dominant Ozone-Depleting Substance Emitted in the 21st Century, *Science*, 326, 123–125, <https://doi.org/10.1126/science.1176985>, 2009.
- Ricard, L., Falasca, F., Runge, J., and Nenes, A.: network-based constraint to evaluate climate sensitivity, *Nature Communications*, 15, 6942, <https://doi.org/10.1038/s41467-024-50813-z>, 2024.

- 930 Runge, J.: Discovering contemporaneous and lagged causal relations in autocorrelated nonlinear time series datasets, in: Proceedings of the 36th Conference on Uncertainty in Artificial Intelligence (UAI), edited by Peters, J. and Sontag, D., vol. 124 of *Proceedings of Machine Learning Research*, pp. 1388–1397, PMLR, <https://doi.org/10.48550/arXiv.2003.03685>, 2020.
- Runge, J.: jakobrunge/tigramite: Tigramite 5.0, <https://doi.org/10.5281/zenodo.6247837>, 2022.
- Runge, J., Petoukhov, V., and Kurths, J.: Quantifying the strength and delay of climatic interactions: The ambiguities of cross correlation and
935 a novel measure based on graphical models, *Journal of climate*, 27, 720–739, <https://doi.org/10.1175/JCLI-D-13-00159.1>, 2014.
- Runge, J., Nowack, P., Kretschmer, M., Flaxman, S., and Sejdinovic, D.: Detecting and quantifying causal associations in large nonlinear time series datasets, *Science Advances*, 5, eaau4996, <https://doi.org/10.1126/sciadv.aau4996>, 2019.
- Runge, J., Gerhardus, A., Varando, G., Eyring, V., and Camps-Valls, G.: Causal inference for time series, *Nature Reviews Earth & Environment*, 4, 487–505, <https://doi.org/10.1038/s43017-023-00431-y>, 2023.
- 940 Serva, F.: Transformed Eulerian mean data from the ERA5 reanalysis (monthly means), <https://doi.org/10.5281/zenodo.7081721>, 2022.
- Serva, F.: Transformed Eulerian mean diagnostics (tem-diag), <https://doi.org/10.5281/zenodo.10180386>, 2023.
- Serva, F., Christiansen, B., Davini, P., von Hardenberg, J., van den Oord, G., Reerink, T. J., Wyser, K., and Yang, S.: Changes in Stratospheric Dynamics Simulated by the EC-Earth Model From CMIP5 to CMIP6, *Journal of Advances in Modeling Earth Systems*, 16, e2023MS003756, <https://doi.org/10.1029/2023MS003756>, e2023MS003756 2023MS003756, 2024.
- 945 Sofieva, V. F., Szlag, M., Tamminen, J., Kyrölä, E., Degenstein, D., Roth, C., Zawada, D., Rozanov, A., Arosio, C., Burrows, J. P., Weber, M., Laeng, A., Stiller, G. P., von Clarmann, T., Froidevaux, L., Livesey, N., van Roozendaal, M., and Retscher, C.: Measurement report: regional trends of stratospheric ozone evaluated using the Merged GRidded Dataset of Ozone Profiles (MEGRIDOP), *Atmospheric Chemistry and Physics*, 21, 6707–6720, <https://doi.org/10.5194/acp-21-6707-2021>, 2021.
- Spirtes, P.: Directed cyclic graphical representations of feedback models, in: Proceedings of the Eleventh Conference on Uncertainty in
950 Artificial Intelligence, UAI'95, p. 491–498, Morgan Kaufmann Publishers Inc., San Francisco, CA, USA, ISBN 1558603859, 1995.
- Spirtes, P., Glymour, C. N., Scheines, R., and Heckerman, D.: Causation, prediction, and search, MIT press, 2000.
- Steinbrecht, W., Froidevaux, L., Fuller, R., Wang, R., Anderson, J., Roth, C., Bourassa, A., Degenstein, D., Damadeo, R., Zawodny, J., Frith, S., McPeters, R., Bhartia, P., Wild, J., Long, C., Davis, S., Rosenlof, K., Sofieva, V., Walker, K., Rahpoe, N., Rozanov, A., Weber, M., Laeng, A., von Clarmann, T., Stiller, G., Kramarova, N., Godin-Beekmann, S., Leblanc, T., Querel, R., Swart, D., Boyd, I., Hocke,
955 K., Kämpfer, N., Maillard Barras, E., Moreira, L., Nedoluha, G., Vigouroux, C., Blumenstock, T., Schneider, M., García, O., Jones, N., Mahieu, E., Smale, D., Kotkamp, M., Robinson, J., Petropavlovskikh, I., Harris, N., Hassler, B., Hubert, D., and Tummon, F.: An update on ozone profile trends for the period 2000 to 2016, *Atmospheric Chemistry and Physics*, 17, 10675–10690, <https://doi.org/10.5194/acp-17-10675-2017>, 2017.
- Szlag, M. E., Sofieva, V. F., Degenstein, D., Roth, C., Davis, S., and Froidevaux, L.: Seasonal stratospheric ozone trends over 2000–2018
960 derived from several merged data sets, *Atmospheric Chemistry and Physics*, 20, 7035–7047, <https://doi.org/10.5194/acp-20-7035-2020>, 2020.
- Thompson, A. M., Stauffer, R. M., Wargan, K., Witte, J. C., Kollonige, D. E., and Ziemke, J. R.: Regional and Seasonal Trends in Tropical Ozone From SHADOZ Profiles: Reference for Models and Satellite Products, *Journal of Geophysical Research: Atmospheres*, 126, e2021JD034691, <https://doi.org/https://doi.org/10.1029/2021JD034691>, e2021JD034691 2021JD034691, 2021.
- 965 Tian, W., Chipperfield, M. P., Gray, L. J., and Zawodny, J. M.: Quasi-biennial oscillation and tracer distributions in a coupled chemistry-climate model, *Journal of Geophysical Research: Atmospheres*, 111, 2006.

- Tibau, X.-A., Reimers, C., Gerhardus, A., Denzler, J., Eyring, V., and Runge, J.: A spatiotemporal stochastic climate model for benchmarking causal discovery methods for teleconnections, *Environmental Data Science*, 1, e12, <https://doi.org/10.1017/eds.2022.11>, 2022.
- 970 Tweedy, O. V., Kramarova, N. A., Strahan, S. E., Newman, P. A., Coy, L., Randel, W. J., Park, M., Waugh, D. W., and Frith, S. M.: Response of trace gases to the disrupted 2015–2016 quasi-biennial oscillation, *Atmospheric Chemistry and Physics*, 17, 6813–6823, <https://doi.org/10.5194/acp-17-6813-2017>, 2017.
- Uleman, J. F., Luijten, M., Abdo, W. F., Vyrastekova, J., Gerhardus, A., Runge, J., Rod, N. H., and Verhagen, M.: Triangulation for causal loop diagrams: constructing biopsychosocial models using group model building, literature review, and causal discovery, *npj Complexity*, 1, 19, 2024.
- 975 United Nations: Montreal Protocol on Substances that Deplete the Ozone Layer, <https://ozone.unep.org/treaties/montreal-protocol>, adopted 16 September 1987, 1987.
- Villamayor, J., Iglesias-Suarez, F., Cuevas, C. A., Fernandez, R. P., Li, Q., Abalos, M., Hossaini, R., Chipperfield, M. P., Kinnison, D. E., Tilmes, S., et al.: Very short-lived halogens amplify ozone depletion trends in the tropical lower stratosphere, *Nature Climate Change*, 13, 554–560, 2023.
- 980 Weber, J., Keeble, J., Abraham, N. L., Beerling, D. J., and Martin, M. V.: Global agricultural N₂O emission reduction strategies deliver climate benefits with minimal impact on stratospheric O₃ recovery, *npj Climate and Atmospheric Science*, 7, 121, 2024.
- Weber, M., Arosio, C., Coldewey-Egbers, M., Fioletov, V. E., Frith, S. M., Wild, J. D., Tourpali, K., Burrows, J. P., and Loyola, D.: Global total ozone recovery trends attributed to ozone-depleting substance (ODS) changes derived from five merged ozone datasets, *Atmospheric Chemistry and Physics*, 22, 6843–6859, <https://doi.org/10.5194/acp-22-6843-2022>, 2022.
- 985 WMO: Scientific Assessment of Ozone Depletion: 2022, Tech. Rep. 278, World Meteorological Organization, Geneva, 2022.
- Wright, S.: Correlation and causation, *Journal of agricultural research*, 20, 557, 1921.
- Zerefos, C., Fountoulakis, I., Eleftheratos, K., and Kazantzidis, A.: Long-term variability of human health-related solar ultraviolet-B radiation doses from the 1980s to the end of the 21st century, *Physiological Reviews*, 103, 1789–1826, <https://doi.org/10.1152/physrev.00031.2022>, pMID: 36787480, 2023.